Atmos. Chem. Phys., 26, 16837–16856, 2026
https://doi.org/10.5194/acp-26-16837-2026
© Author(s) 2026. This work is distributed under
the Creative Commons Attribution 4.0 License.

Atmospheric Chemistry and Physics
Open Access
EGU

Measurement report: Geostationary satellite and ground-based video observations of cloud brightness variations triggered by the 2022 Hunga Lamb wave

Ákos Horváth[1], David K. Adams[2], Jorge S. Díaz[3], Sam E. Rigby[4], Stefan A. Buehler[5], and Mirjana Sakradzija[6]

[1]Institute of Meteorology and Climate Research – Troposphere Research (IMKTRO), Karlsruhe Institute of Technology (KIT), Karlsruhe, Germany
[2]El Instituto de Ciencias de la Atmósfera y Cambio Climático, Universidad Nacional Autónoma de México, Mexico City, Mexico
[3]Department of Physics, Indiana University, Bloomington, Indiana, USA
[4]School of Mechanical, Aerospace and Civil Engineering, University of Sheffield, Sheffield, UK
[5]Department of Earth System Sciences, University of Hamburg, Hamburg, Germany
[6]Department of Geography, Ludwig-Maximilians Universität, München, Germany

Correspondence: Ákos Horváth (hfakos@gmail.com)

Received: 5 July 2026 – Discussion started: 4 August 2026
Revised: 7 October 2026 – Accepted: 2 November 2026 – Published: 25 November 2026

Abstract. The eruption of the Hunga volcano on 15 January 2022 generated a Lamb wave, an atmospheric pressure perturbation propagating horizontally at the speed of sound. A recent regional study uncovered variations in the reflectance of liquid clouds triggered by the wave's temperature perturbations, most notably a transient darkening during the first minor-arc wave passage across the Caribbean. The present expanded analysis – combining ground-based video footage, surface pressure records, and geostationary satellite imagery – reveals that the Lamb wave-induced cloud reflectance variations were globally detectable for ∼6 d. Reflectance anomalies traced temperature anomalies on timescales as short as a few seconds to 1 min and persisted at the 2 % level even after 3 d of propagation. The relative magnitudes of cloud darkening and brightening changed upon each crossing of the antipode or the epicenter due to the caustic phase shift. Brightening dominated during the second minor-arc wave passage because of a polarity inversion. The observed lifetime of the Lamb wave compares well with early theoretical estimates.

1 Introduction

The extraordinary eruption of the Hunga submarine volcano on 15 January 2022 produced planetary-scale disturbances. The estimated energy release of the eruption ranges from 61–200 Mt of trinitrotoluene (TNT) equivalent (Adushkin et al., 2022; Díaz and Rigby, 2022b; McNutt et al., 2026; Vergoz et al., 2022), placing it above the 1961 Tsar Bomba thermonuclear test, the largest human-made explosion (50–58 Mt; Sublette, 2007) and the 1991 Mount Pinatubo eruption (30–70 Mt; Díaz and Rigby, 2022b; Tahira et al., 1996), being energetically comparable to the 1883 Krakatoa eruption (150–200 Mt; Harkrider and Press, 1967; Yokoyama, 1981). The highest overshoot of the Hunga plume reached the mesosphere at an altitude of 55–58 km (Carr et al., 2022; Proud et al., 2022), which is below the ∼80 km height of the Krakatoa plume (Britannica Editors, 2026) and the 64–67 km height of the Tsar Bomba mushroom cloud (Sublette, 2007; Wellerstein, 2021), but well above the ∼40 km height of the Pinatubo plume (Holasek et al., 1996), making Hunga the tallest plume observed in the satellite era. The eruption ejected a record amount of water vapor (WV) into the stratosphere, estimated at ∼150 Tg or ∼10 % of the total strato-

spheric WV burden (e.g., Millán et al., 2022). Modelling studies indicate that the plume's remarkable ascent was propelled by steam-driven convection with water phase changes playing a crucial role (Mastin et al., 2024; McNutt et al., 2026). The eruption's effects on atmospheric composition, circulation, radiative forcing, and climate are summarized in a comprehensive impact report (APARC, 2025).

Most pertinent for the current study, the rapidly rising eruption column generated a broad spectrum of atmospheric waves, including gravity waves (GWs; e.g., Matoza et al., 2022), a prominent Lamb wave (e.g., Horváth et al., 2024; Wright et al., 2022), and an elusive Pekeris wave, detected for the first time (Pekeris, 1937; Watanabe et al., 2022). The Lamb and Pekeris waves are horizontally propagating pressure waves, representing two normal modes of the atmosphere. The Lamb wave is a surface-guided acoustic wave which is vertically in-phase and whose energy density decays exponentially with height (Bretherton, 1969; Garrett, 1969). It travels at the speed of sound, with observed long-distance averages for Hunga typically ranging between 310–320 $\mathrm{m\,s^{-1}}$ (e.g., Vergoz et al., 2022; Wright et al., 2022). The Lamb wave's local propagation, however, is affected by winds and topography, leading to significant regional speed variations and consequent far-field distortions of the initially concentric wavefronts (Sepúlveda et al., 2023). The Pekeris wave is a weaker and slower ducted wave propagating at $\sim 245\,\mathrm{m\,s^{-1}}$, which undergoes a 180° phase shift in the lower stratosphere and whose energy density peaks in the upper stratosphere and the mesosphere (Salby, 1979; Watanabe et al., 2022).

The wave-induced compression–rarefaction perturbations and the corresponding warming–cooling anomalies produced globally observable signals in surface pressure and satellite brightness temperatures (BTs). The Lamb wave was found to have circled the Earth two to three times in pressure records (Dalal et al., 2023; Matoza et al., 2022) and five to six times in satellite BTs (Otsuka, 2022), and the Pekeris wave was tracked in BTs to at least Japan, 8000 km from Hunga (Watanabe et al., 2022). The research community devoted most of its attention to the surface and upper-atmospheric effects of the Hunga waves, with numerous studies investigating the meteotsunamis driven by the Lamb wave (e.g., Kubota et al., 2022; Purkis et al., 2023) or the traveling ionospheric disturbances generated by secondary GWs (e.g., Harding et al., 2022; Vadas et al., 2023).

In contrast, only two studies, Horváth et al. (2025) and Prata et al. (2025), to date have explored the impact of the Hunga waves on meteorological clouds. Horváth et al. (2025) analyzed Geostationary Operational Environmental Satellite-16 (GOES-16) imagery of the Lamb wave's first daytime passage across the Continental US (CONUS) sector. These far-field observations, 9000–12 000 km from Hunga, revealed synchronized variations in the solar reflectance (R or brightness) of low-level liquid clouds, most notably a transient darkening accompanying the Lamb wave's dominant compression peak. Horváth et al. (2025) hypothesized that the brightness variations were caused by the rapid thermodynamic adjustment of the cloudy environment to the warming and cooling perturbations associated with the pressure wave. The ensuing oscillations in relative humidity led to the alternating shrinkage–evaporation and growth–condensation of small cloud droplets and near-cloud hygroscopic aerosols, which, in turn, modulated the optical thickness of the cloudy column.

Prata et al. (2025) documented similar near-field effects of Pekeris wave-induced temperature variations on ice particle formation. Analyzing Himawari-8 BTs in the first few hours of the eruption, they showed that the cooling during the negative wave phase produced a transient ice ring (TIR) around the plume, comprising small ice particles with a mean effective radius of $\sim 2\,\mu\mathrm{m}$. The ice crystals grew via vapor deposition in an atmosphere supersaturated with respect to ice. The TIR formed at an altitude of 16–18 km in the upper troposphere–lower stratosphere, where the Pekeris wave's amplitude is larger than in the troposphere. The ice ring appeared ~ 40 min after the eruption, reached its maximum radius of ~ 300 km in half an hour, and dissipated within ~ 2 h.

Expanding upon the spatiotemporally limited study of Horváth et al. (2025), here we document global cloud brightness variations triggered by the Lamb wave over a multi-day period using ground-based video and geostationary satellite observations. Results are presented in order of increasing distance and time from the eruption, starting with near-field video footage from Nuku'alofa, Tonga (~ 73 km from Hunga), sampled at 2 s intervals. Middle-field effects are analyzed in the 1 min cadence GOES-17 mesoscale domain centered on American Samoa (~ 200–1600 km from Hunga). Finally, far-field effects are identified globally in geostationary-ring images, using 10 min cadence full-disk and 5 min cadence regional scans. By comparing satellite observations with surface pressure records captured at propagation distances ranging from a few hundred to tens of thousands of kilometers, we establish a persistent connection between pressure anomalies and cloud brightness variations. We also demonstrate that Lamb wave-induced perturbations remain visually detectable in low-level cloud reflectance for 5–6 d and in thermal infrared BTs for 7–8 d following the eruption.

The report is organized as follows. In Sect. 2, we describe the surface pressure data, the ground-based video footage, and the visualization of the Lamb wave in satellite images. In Sect. 3, we track the Lamb wave's effect on clouds during two full global circumnavigations over a 3 d period. Section 4 concludes the report with a discussion and summary.

2 Data and methods

2.1 Surface pressure waveforms

The Lamb wave left an imprint in surface pressure that was detectable worldwide for about 6 d (Matoza et al., 2022).

We use seismic-style naming conventions to track the multi-orbit Lamb wave passages. Odd-numbered arrivals (L1, L3, L5) correspond to the minor-arc wavefront traveling along the shortest direct path from the source; L1 is the first direct passage, whereas L3 and L5 represent the second and third passages following full global circuits. Similarly, even-numbered arrivals (L2, L4, L6) denote the major-arc wavefront traveling in the opposite direction along the longest path from the source. L2 represents the initial major-arc arrival, and subsequent even phases mark the completion of successive full laps around the globe.

Here, we focus on two pressure records which represent daytime wave passages on 15 and 17 January, bracketing nearly two full global circuits of the Lamb wave. The geographic locations of the Nu'uuli and Santa Barbara datasets are shown in Fig. 1. Pressure was recorded at 1 min intervals at both locations, permitting the accurate characterization of the waveform and the wave's arrival time. The middle-field record on 15 January is from the personal weather station of J. LaPlante, sited at Coconut Point in Nu'uuli (Tutuila Island, American Samoa), $\sim$850 km from Hunga (Supplement S1). This dataset captures the initial (zonally west-to-east propagating) L1 minor-arc passage of the wave. The far-field record on 17 January is from the Automated Surface Observing System (ASOS; NOAA, 2005) weather station at Santa Barbara Municipal Airport (identifier SBA or KSBA, Santa Barbara, CA), $\sim$8456 km from Hunga. This dataset captures the second antipodal (zonally east-to-west propagating) L4 passage, corresponding to a total travel distance of $\sim$71 544 km.

The pressure anomalies for the two stations are plotted in Fig. 2. The magnitude of the anomalies is somewhat sensitive to the specific method used to detrend the raw data; while this choice determines the pressure baseline, it does not significantly affect the wave morphology. Here, we chose a detrending method separately for the two datasets, which yielded minimal anomalies prior to the arrival of the Lamb wave packet. The Nu'uuli anomalies were calculated by subtracting a 5th-order polynomial fit from the pressure (excluding the 05:00–05:45 UTC wave passage from the fit), while the Santa Barbara anomalies were calculated by subtracting a 35 min moving average from the pressure. The spectral analysis of Hunga barograph records indicates a primary, broad energy maximum at periods of 30–50 min (e.g., Horváth et al., 2024; Matoza et al., 2022; Vergoz et al., 2022). A first-order estimate based on the time difference between the main peak and the first trailing peak yields a Lamb period of 31 min for the pressure data in Fig. 2.

The morphology of the far-field Lamb wave, however, is substantially affected by other factors, chief among them is the polar phase shift (Brune et al., 1961; Wielandt, 1980). The phase of spherical surface waves advances by $\pi/2$ (90° or a quarter wavelength) upon each passage through the epicenter or antipode (caustics), which alters the waveform appearance by introducing a shift to the arrival times of peaks and troughs. Neglecting the polar phase shift leads to a systematic bias in phase velocities derived from waveform matching across caustic crossings or multiple orbits. Variations in wind and temperature (i.e., speed of sound) along the travel path also modify phase arrival times and, as such, can be considered an effective phase shift. Finally, the slight dispersion of the Lamb waves separates the lower-frequency and higher-frequency components and, thus, broadens the wave packet over large distances.

Crucially, an initial phase advance of $\pi/4$ (45°) occurs for two-dimensional surface waves propagating away from a point source (Brune et al., 1961). This initial phase shift is largely responsible for the formation of the trailing low-pressure trough behind the primary compressional pulse, and it must be accounted for when inverting the source time function from far-field records. For the Hunga eruption, violent volcanic updrafts additionally generated a low-pressure zone that dynamically altered near-field waveforms. While these near-source hydrodynamic complexities remain outside the framework of the current study, accounting for the cumulative polar phase shift is sufficient when evaluating the relative phase relationships across our barographic datasets.

The L1 waveform is characterized by two low-amplitude precursors followed by a sharp primary pressure pulse, a prominent trough approximately 12 min later, and a $\sim$20 min recovery phase. The peak–trough sequence is typical of minor-arc pressure anomalies observed worldwide on 15 January. In contrast, the L4 waveform recorded on 17 January exhibits a small peak followed by a trough–peak–trough sequence, reflecting the morphological transformation caused by the 270° phase advance accumulated over three caustic crossings (antipode–epicenter–antipode). The L4 peak and troughs are also broadened compared to L1, likely due to dispersion. Another consequence of the polar phase shift is that, all things being equal, the L4 pressure peak arrives a quarter cycle or $\sim$10 min later than what is theoretically expected for a given phase speed. This leads to a slightly overestimated travel time and underestimated mean phase speed between the L1 and L4 pressure peaks. The speed underestimation, however, is only $\sim$0.81 m s^{-1} (307.95 vs. 308.76 m s^{-1}) or $\sim$0.3 %. Although the velocity bias induced by the caustic phase shift is larger over shorter paths, it remains negligible compared to the uncertainties caused by atmospheric conditions (wind and temperature variations). Also, note that the pressure perturbations and the resulting adiabatic temperature perturbations remain in-phase even after the caustic shift.

In addition to the change in waveform shape, the amplitude of the pressure anomalies decreased by an order of magnitude between L1 and L4. Nevertheless, the compression is stronger than the rarefaction in both records (+5.4 vs. −4.1 hPa for L1 and +0.6 vs. −0.3 hPa for L4), an asymmetry noted before (Horváth et al., 2025; Watada et al., 2023). Such asymmetry between the magnitudes of the positive and

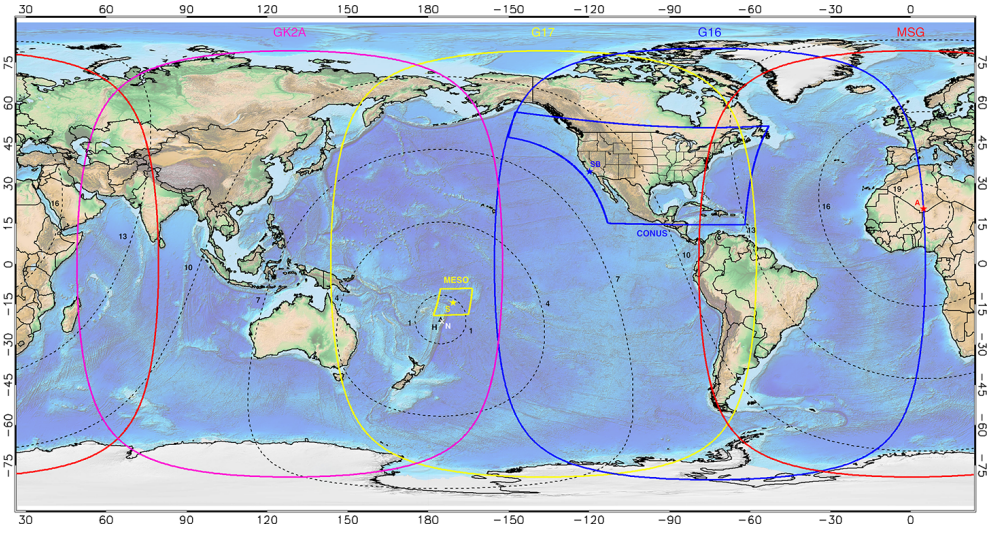

Figure 1. Geographic locations of the datasets used for tracking the Lamb wave from Hunga (H, black triangle). Barograms: Nu'uli, American Samoa (S, yellow star), Santa Barbara (SB, blue star). Ground-based video: Nuku'alofa (N, white ×). Geostationary satellite coverage is marked by colored lines. GOES-17 (G17, yellow): full disk, mesoscale (MESO). GOES-16 (G16, blue): full disk, Continental US (CONUS). Meteosat Second Generation (MSG, red): full disk. GEO-KOMPSAT-2A (GK2A, magenta): full disk. The red star is Hunga's antipode (A) and black dotted lines are epicentral distances (×1000 km). The background map is the ETOPO 2022 Global Relief Model (MacFerrin et al., 2025).

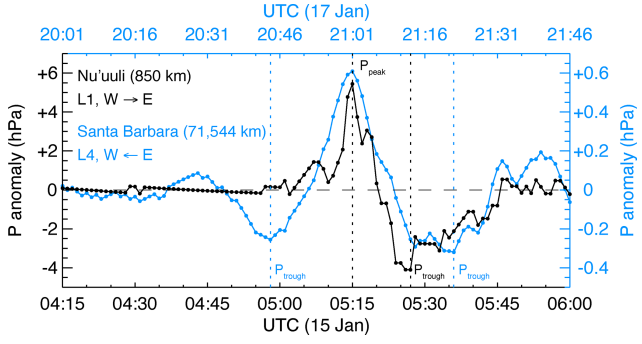

Figure 2. Pressure anomalies recorded at 1 min resolution for Nu'uli (14.32° S, 170.70° W; black) and Santa Barbara (34.43° N, 119.84° W; blue) on 15 and 17 January, respectively. The Nu'uli barogram captures the initial L1 passage, while Santa Barbara shows the L4 passage after three caustic crossings. The arrival times of the main pressure peak and pressure troughs, P_{peak} and P_{trough}, are also marked.

negative pressure phases is typical of blast waves from controlled explosions (Bonner et al., 2013; Fee et al., 2013).

2.2 Ground-based video

We used a ground-based video from Nuku'alofa (21.13° S, 175.20° W), Tongatapu, Tonga, ∼ 73 km southeast of Hunga, recorded by B. M. MacDonald (MacDonald, 2022). The 20 min footage combines various clips from a GoPro camera, an iPhone, and a Canon DSLR (Digital Single-Lens Reflex) camera, collected intermittently over the first few hours after the eruption between ∼ 05:22–09:02 pm local Tonga Time (∼ 04:22–08:02 UTC) on 15 January. We focused on a continuous video segment between ∼ 05:28–05:30 pm local Tonga Time (∼ 04:28–04:30 UTC), captured by the Hunga-facing Canon camera at 30 fps (frames per second), but here sampled at every 2 s. The footage includes time stamps (Tonga Time) with an estimated accuracy of 1–2 min as well as occasional barometer readings. The observer also provides a running commentary, pointing out notable events such as tremors and loud booms, pressure fluctuations and the corresponding changes in low-level clouds, wind speed variations, and tephra fallout. The time-resolved pressure readings in this video formed part of the dataset from which Díaz and Rigby (2022b) derived an empirical pressure–distance relation to estimate the energetic output of the eruption (∼ 61 Mt). Additional videos posted on social media also vividly captured near-field cloud fluctuations caused by the Hunga pressure waves (e.g., Barnaboule69, 2022), but none are time-stamped and as comprehensive as the one analyzed in our study.

2.3 Geostationary satellite imagery

The coverage areas of Level 1 imagery used in our study are depicted in Fig. 1: GK2A located at 128.2° E (Korea Meteorological Administration, 2019), GOES-17 at 137.2° W (GOES-R, 2017), GOES-16 at 75.2° W (GOES-R, 2017), and MSG at 0° (EUMETSAT, 2009). All satellites provide full disk (FD) images, the first three at 10 min cadence and MSG (Meteosat-11) at 15 min cadence. Additionally, the

GOES-16 CONUS scans are available at 5 min cadence and the GOES-17 MESO scans at 1 min cadence. The GK2A image slot at 00:40 UTC is consistently missing between 15–23 January 2022, likely due to instrument maintenance. Data are also available from Himawari-8 (140.7° E); however, we here opted for GK2A, which covers the same general area, but in our experience provides slightly sharper and better georegistered images for tracking the Hunga Lamb wave. Note that the Horváth et al. (2025) analysis was limited to the GOES-16 CONUS domain on 15 January.

The GK2A and GOES-R satellites host nearly identical, 16-channel imagers: the Advanced Meteorological Imager (AMI) and the Advanced Baseline Imager (ABI), respectively. Their solar reflectance channels have nominal resolutions ranging between 0.5–2.0 km and all their emissive channels have a 2.0 km resolution. The MSG satellite hosts the 12-channel Spinning Enhanced Visible Infra-Red Imager (SEVIRI) instrument, with its 11 narrowband channels having a 3 km nominal resolution.

As in previous studies, we visualize the Lamb wave by taking the second time derivative of brightness temperature and reflectance, denoted by BT″ and R″ (e.g., Horváth et al., 2024; Otsuka, 2022; Wright et al., 2022). The BT″ and R″ images are then grayscaled, spatially smoothed with a boxcar filter, and histogram equalized to increase contrast. Two points are worth noting here. One, the time derivative constitutes a high-pass filter, which diminishes longer-period background variations and emphasizes the signal from fast-propagating waves. Thus, the resulting images depict the "acceleration" of BT and R, with negative and positive accelerations rendered as black and white stripes, respectively. The sign of the second derivative specifies the concavity ("bend") of the time series curve: < 0 concave down and > 0 concave up, which often also indicates local maxima and minima in temperature or reflectance.

Two, the visibility of the Lamb wave across the image depends on the geographic distribution of the atmospheric constituents to which a specific channel is sensitive. In solar reflectance and infrared (IR) window channels, the wavefront is only detectable in areas with low-level clouds, often resulting in a fragmented visual expression. Conversely, the wavefront appears spatially continuous in the WV (6.3, 6.9, 7.3 µm) and ozone (9.6 µm) channels, providing a more coherent signal for global tracking. Also note that the GOES-17 ABI suffered a loop heat pipe anomaly, which occasionally leads to significant noise and striping artifacts in the IR imagery (McCorkel et al., 2019).

3 Lamb wave cloud effects

3.1 Near field

3.1.1 Shock wave to Lamb wave

Before analyzing the observed cloud effects of the Hunga Lamb wave, we briefly discuss the shock wave to Lamb wave transition; additional details are given in Appendix A. An explosive pressure wave begins as a finite-amplitude shock governed by nonlinear gas dynamics, with overpressures reaching several atmospheres and the wavefront propagating at supersonic speeds (Neumann, 1963; Sedov, 1993; Taylor, 1950). The wave expands quasi-spherically (modified by the ground boundary into a hemispherical geometry), heating the air as it decelerates. The amplitude decay with increasing radius r exceeds the $1/r$ geometric spreading of linear waves due to nonlinear steepening and shock dissipation (Kinney and Graham, 1985).

As the shock diminishes with distance, the peak overpressure falls toward ambient atmospheric values and the nonlinear disturbance transitions into linear acoustic–gravity modes. The atmosphere supports several wave types simultaneously in this regime, but the dominant and longest surviving signal is the Lamb mode, which propagates horizontally at the local speed of sound. Most importantly for our discussion, the shock decay occurs within a short distance even for the largest explosions. For the estimated 61–200 Mt energy release of Hunga, the relaxation radius is only $\sim$8–12 km (Appendix A).

The detection of the supersonic shock front is nontrivial. When clouds are present, it might be detected by the evaporation of clouds due to the elevated temperature. In clear skies, a visible optical phenomenon known as "flashing arcs" can be occasionally observed behind shock fronts (Czarnecki et al., 2026; Genco et al., 2014; Nairn, 1976). They manifest as a rapidly moving arc of increased luminosity or hue variations caused by the increased refractive index of the high-density air.

A far more common observation is the formation of condensation clouds or Wilson clouds in the rarefaction phase. If the ambient relative humidity is at least 70 %, the sudden adiabatic cooling can temporarily drive the relative humidity to supersaturation, leading to the condensation of visible clouds (Waltz, 1978). Note that pressure and temperature variations exert opposite effects on relative humidity; however, the exponential temperature dependence of saturation vapor pressure dominates. Wilson clouds were observed in nuclear tests (e.g., atomcentral, 2016), the 2020 Beirut explosion (Czarnecki et al., 2026; Díaz, 2021; Zéhil, 2024), and the 1975 Ngauruhoe volcano eruption (Nairn, 1976). Although cloud lifetime increases with higher ambient relative humidity, the evaporation of shock wave condensation clouds is generally very fast, typically occurring in 1–3 s. Such transient Wilson clouds produced by small volcanic eruptions have been documented in several amateur videos posted on social media

(e.g., Abyssius, 2014; afarTV, 2025; ArchiveRandom, 2025; we recommend a video playback speed of 0.25× or 0.50×).

We hypothesize that the paroxysmal Hunga explosion also generated a localized shock wave. However, observational evidence is lacking, because this supersonic, high-overpressure wave was short-lived and relaxed into an acoustic wave within ∼ 10 km of the vent. The 10 min cadence full-disk imagery could not capture this rapid phenomenon. The closest high-cadence measurements were collected an order of magnitude further away in Nuku'alofa, ∼ 73 km from the source. Although many media accounts described the global pressure pulse and the satellite observations of expanding concentric BT rings as a "shock wave", these far-field signals were in fact due to the guided Lamb mode or gravity waves, not the shock wave. The loud bangs heard in locations as distant as New Zealand and Alaska were likewise mislabeled in some accounts as "sonic booms," a term that properly refers to the N-wave overpressure signature produced by an object moving through air faster than the local speed of sound, e.g., a supersonic aircraft (Whitham, 1952). No such source existed at these distances; thus, the audible bangs instead represent direct acoustic arrivals of infrasonic and low-frequency sound energy generated at the vent, refracted and channeled through atmospheric waveguides before arriving at the surface with enough amplitude to be perceptible to the human ear. These sound propagation pathways are well documented for large explosive sources including volcanic eruptions and bolides (Evers and Haak, 2001; Le Pichon et al., 2019).

3.1.2 Nuku'alofa, 15 January, L1

The eruption chronology and early plume evolution have been extensively covered in the literature (e.g., Carr et al., 2022; Gupta et al., 2022; Proud et al., 2022). Here we first present a few satellite snapshots which set the stage for the global propagation of the Lamb wave, reveal near-field cloud formation–evaporation and, thus, give context for the interpretation of the ground-based video footage. Figure 3 shows plume development between 04:37–05:07 UTC captured in the highest-resolution GOES-17 channel 2 FD images (0.5 km resolution, 0.64 µm visible red band). In an FD image, Hunga is observed ∼ 7 min after the scan start time used for time stamping the data files. As visual aid, we also indicate the locations of L1 waveform features back-propagated to the imaging time assuming a mean phase speed between Nu'uli and Hunga of 315 m s^{-1}. Because the propagation speed can vary along the path due to the initial supersonic shock wave decelerating to an acoustic wave or because of local winds, the waveform guidelines are only approximate.

At 04:37 UTC, the plume attained its highest observed altitude with the top of the central dome being at 56–57 km and Nuku'alofa was already under the umbrella. The main Lamb pulse (solid red line) generated at ∼ 04:29 UTC (Horváth et al., 2024) was beyond Nuku'alofa by that time, as it had reached the city at ∼ 04:33 UTC after a ∼ 4 min travel from the epicenter. The area within ∼ 300 km of Hunga was largely cloud-free, only containing scattered cumulus at 2–4 km altitude (Carr et al., 2022). 10 min later, the central dome collapsed and the umbrella was spreading near ∼ 30 km altitude. More importantly, a ring of low-level clouds formed around the volcano in humid air exposed to the negative, cooling phase of the Lamb wave. The radial extent of this cloud ring was well bounded by the zero-crossing after the main pressure pulse (dotted black line, ∼ 217 km from Hunga), where compression turned into rarefaction. The passage of the Lamb overpressure peak, however, reduced cloudiness further away from the volcano. For example, the patch of thin clouds marked by the white arrow (⇒) largely evaporated between 04:37 and 04:47 UTC due to the compressional warming of air.

By 04:57 UTC, the entire area within ∼ 400 km of Hunga was experiencing the cooling phase of the Lamb wave,

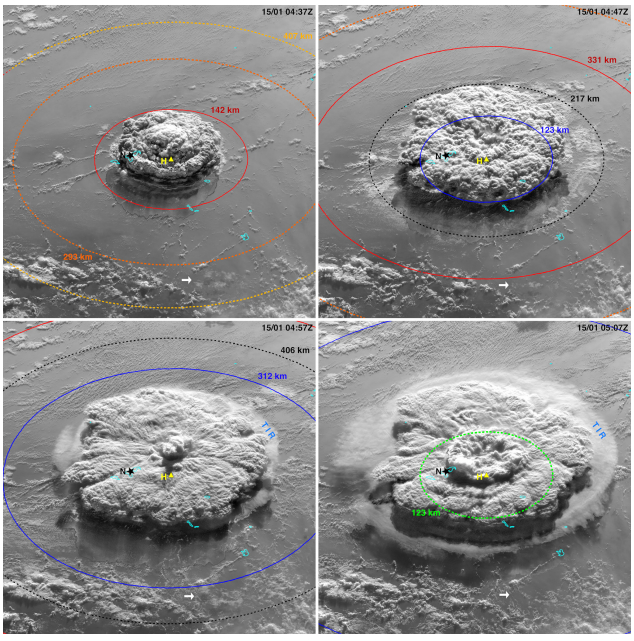

Figure 3. GOES-17 channel 2 FD snapshots of the plume between 04:37–05:07 UTC on 15 January (the images are rotated clockwise by 120°). Hunga (H, yellow triangle), Nuku'alofa (N, black star), and the transient ice ring (TIR) are also marked. The curves indicate the positions of select features of the Nu'uli pressure anomaly (Fig. 2) back-propagated to the FD imaging times. The features are identified by their arrival times at Nu'uli: 1st peak at 05:01 UTC (dotted light orange), 2nd peak at 05:07 UTC (dotted orange), main peak at 05:15 UTC (solid red), zero-crossing at 05:21 UTC (dotted black), main trough at 05:27 UTC (solid blue), and recovery at 05:46 UTC (dotted green). The white arrow points to a cloud patch that partially evaporates, recondenses, and dissipates during the passage of the wave. Shadowed areas were enhanced by the Contrast Limited Adaptive Histogram Equalization (CLAHE) plugin of the Fiji package (Schindelin et al., 2012).

with the main rarefaction trough (solid blue line) located ∼312 km from the volcano. Cloudiness considerably increased in this region through condensation in clear air or the expansion of preexisting clouds, including the recondensation of the patch marked by the arrow. Also note the appearance of the transient ice ring described by Prata et al. (2025), which formed near the tropopause (∼17 km altitude) during the negative phase of the slower-moving Pekeris wave. By 05:07 UTC, the TIR expanded further, but some of the previously formed liquid clouds (including the patch at the arrow) dissipated as the pressure started to increase (the location of the Lamb wave pressure recovery is indicated by the dotted green line).

The ground-based video from Nuku'alofa includes several instances of clouds shrinking and growing due to pressure wave-induced temperature fluctuations. One of the clearest cases is a ∼2 min clip between ∼04:28–04:30 UTC, which captures a couple of shrinkage–growth cycles and shows the cloud base rising and dropping (video project time 00:04:28–00:06:48, given in HH:MM:SS format, where HH, MM, and SS are the two-digit hour, minute, and second, respectively). As an example, Fig. 4 plots frames centered on a cumulus patch and sampled every 2 s during a 22 s segment (video project time 00:04:46–00:05:08). We manually tracked the central cloud to compensate for the left-to-right cloud motion. The clouds noticeably shrink during the 10 s between panels S1–S6 and then regrow in the subsequent 10 s between panels G1–G6.

Because Fig. 4 does not capture a full growth–shrinkage–growth cycle, we calculated variations in image brightness for an extended 60 s period (video project time 00:04:28–00:05:28), which includes the Fig. 4 frames in the middle of the interval. Figure 5 depicts the time evolution of the mean intensity of the sky portion of frames in the red (R), green (G), and blue (B) bands, and the variation of the mean luminance, defined in GIMP as $0.222\times R+0.717\times G+0.061\times B$. The video footage revealed brightness fluctuations with a period of ∼40 s, resulting from the varying cloud amount. Such high frequency oscillations cannot be captured in the 1 min cadence surface pressure data or GOES-17 MESO scans. Note the dip in image brightness at video project time 00:05:14, caused by a bird flying into the frame (birds can also be seen in the last four frames in Fig. 4).

The cloud fluctuations captured by the Nuku'alofa video around ∼04:28 UTC appear unrelated to the primary Lamb pulse, which likely reached the city a few minutes later at ∼04:33 UTC. Instead, these variations were probably driven by the lower amplitude precursor observed in the Nu'uuli pressure trace at 05:07–05:08 UTC (Fig. 2). Considering a ∼45 min travel time to Nu'uuli (assuming a phase speed of 315 m s^{-1}), this precursor left Hunga at ∼04:22–04:23 UTC and reached Nuku'alofa at ∼04:26–04:27 UTC after a ∼4 min travel, consistent with the video footage. A loud boom is also audible in the footage at ∼04:25 UTC (video project time 00:03:23), which again is consistent with



Figure 4. Video frames taken by the Canon DSLR camera in Nuku'alofa (21.13°S, 175.20°W; MacDonald, 2022). During this 22 s period, panels S1–S6 and G1–G6 capture the shrinking and growing cloud phases, respectively. To improve contrast and color depth, the original frames were adjusted by applying the "Stretch Contrast HSV" command in GIMP (GNU Image Manipulation Program; The GIMP Development Team, 2026).

a precursor triggered at Hunga around ∼04:21 UTC. When interpreting this approximate timeline, several limitations must be noted: the video timestamps are accurate only to within 1–2 min, and uncertainties exist regarding both the phase speed estimates and the exact origin time of the main explosion (e.g., Díaz and Rigby, 2022b; Matoza et al., 2022; Gusman and Tanioka, 2025; Wright et al., 2022). Moreover, a precise calculation requires explicitly accounting for the initial phase advance.

The arrival of the primary Lamb pulse is likely represented in the video between project times 00:07:25–00:07:37. Readings by a dial type aneroid barometer during this 12 s period indicate a rapid, 12 hPa rise in air pressure from 993 to 1005 hPa, or a pressure tendency of +1 hPa s^{-1}. The loudest audible boom occurs at the end of this period at video project time 00:07:38. In the next 17 s (video project times 00:07:38–00:07:55), the pressure drops by 7 hPa from 1005 to 998 hPa, corresponding to a tendency of −0.4 hPa s^{-1}. Assuming adiabatic processes, a compression and rarefaction of such magnitudes result in a warming of ∼1.2 K and cooling of ∼0.7 K in the boundary layer (∼0.1 K hPa^{-1}; Horváth et al., 2025;

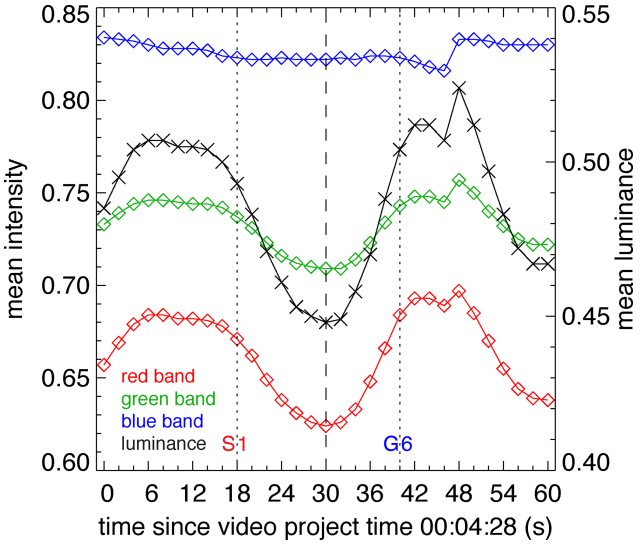

Figure 5. Variation of red, green, and blue band image intensity and image luminance between video project times 00:04:28–00:05:28. The original frames were used without HSV contrast stretch. The period depicted in Fig. 4 is marked by the dotted vertical lines (S1–G6).

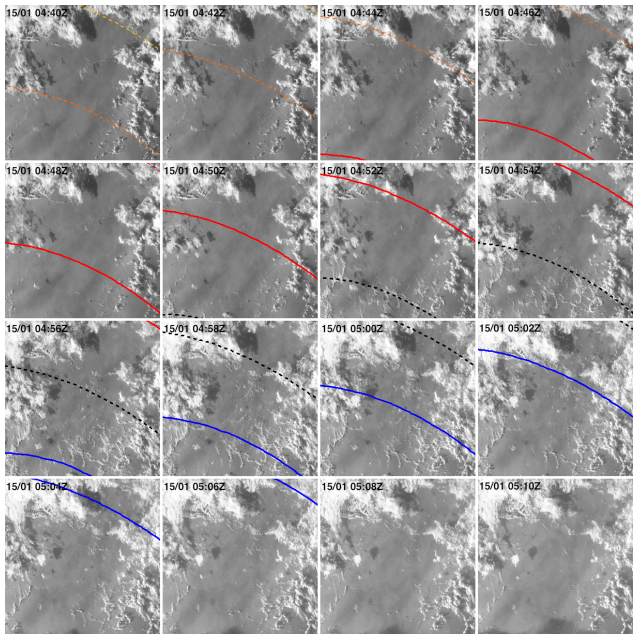

Figure 6. 300 × 300 px (150 × 150 km^2) subset of GOES-17 channel 2 MESO images between 04:40–05:10 UTC on 15 January, sampled at every 2 min. The curves indicate the positions of select features of the Nu'uli pressure anomaly (Fig. 2) back-propagated to the MESO imaging times. The features are identified by their arrival times at Nu'uli: 1st peak at 05:01 UTC (dotted light orange), 2nd peak at 05:07 UTC (dotted orange), main peak at 05:15 UTC (solid red), zero-crossing at 05:21 UTC (dotted black), and main trough at 05:27 UTC (solid blue).

Watada et al., 2023). These warming and cooling anomalies were also accompanied by decreasing and increasing cloudiness, respectively. The compression–rarefaction asymmetry observed here (that is, larger and faster pressure rise) is consistent with that found in the Nu'uli record (Sect. 2.1 and Fig. 2).

To put the Lamb wave pressure tendencies in context, we note that the most extreme pressure drop ever measured, a 100 hPa deficit in 12 s or −8.3 hPa s^{-1}, occurred in the eye of an F4 tornado in Manchester, South Dakota on 24 June 2003; after the eye's passage, the pressure rose at a nearly identical rate (Karstens et al., 2010). The record intensification rates of tropical cyclones, on the other hand, are two orders of magnitude smaller: −9 hPa h^{-1} for Hurricane Wilma (2005; Chen et al., 2011) and −4.3 hPa h^{-1} for Supertyphoon Forrest (1983; Hoarau, 2000).

3.2 Middle field, American Samoa, 15 January, L1

We tracked the further propagation of the Lamb wave in the GOES-17 MESO domain, centered on American Samoa to the northeast of Hunga (Fig. 1). The dataset provides 1 min cadence imagery in a ∼ 1000 × 1000 km^2 area (∼ 200–1600 km from Hunga) between 02:41–05:59 UTC on 15 January. Supplement Animation 1 shows channel 2 (0.64 µm visible red band) reflectances at full resolution (0.5 km) from 04:00 UTC until sunset at 05:59 UTC. The primary pressure peak enters the bottom-left part of the domain at ∼ 04:39 UTC, 10 min after it was triggered near the volcano. As the warming anomaly of the pressure peak propagates northeastward, it partially evaporates low-level clouds. The cooling phase (zero-crossing) of the Lamb wave enters the domain at ∼ 04:45 UTC and leads to the formation of liquid clouds in its wake. These newly formed clouds then start to dissipate as the pressure recovers and temperature rises.

The presence of transient condensation clouds was previously noted in FD images (Fig. 3); however, the MESO data capture their formation and dissipation in much finer temporal detail. Figure 6 plots an area in the bottom (southern) part of the MESO images over a 30 min period, sampled at every 2 min. Low-level condensation clouds start to develop in previously clear regions as the cooling phase of the Lamb wave sweeps through the area. Cloud formation is strongest between the zero-crossing (dotted black line) and the main trough (solid blue line), where temperature drops the fastest. As pressure and temperature slowly recover behind the main trough, clouds dissipate in 10–15 min (e.g., compare panels 04:58 and 05:10 UTC in Fig. 6).

As demonstrated above, transient condensation clouds are plainly visible in raw video and satellite imagery within a few hundred kilometers of Hunga. Taking the second time derivative of images, however, allows detecting even subtle changes in clouds at large distances. Supplement Animation 2 shows BT_{11}'' (8.5 µm cloud-top phase band) and R_{02}'' (0.64 µm visible red band) side by side for the same 2 h

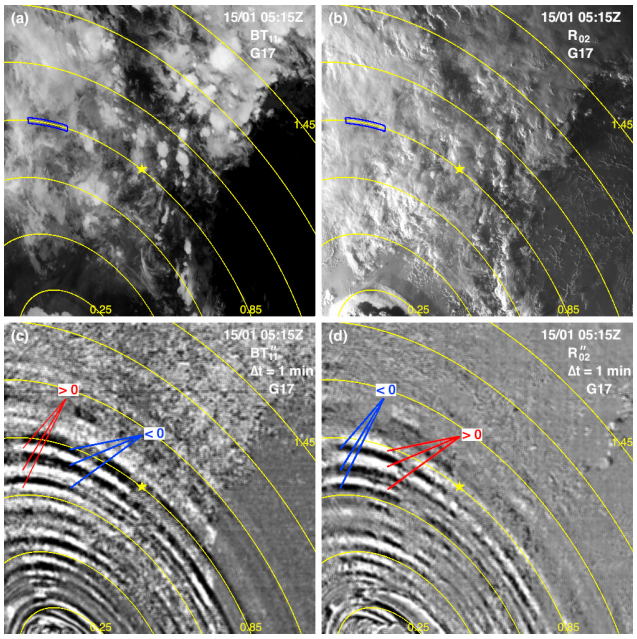

Figure 7. GOES-17 MESO images at 05:15 UTC on 15 January. **(a)** BT_{11}, **(b)** R_{02}, **(c)** BT_{11}'', and **(d)** R_{02}''. The second time derivatives are calculated for $\Delta t = 1$ min. The yellow star is Nu'uuli and the blue domain is the cloudy area analyzed in Fig. 8. The yellow lines are epicentral distances ($\times$ 1000 km) drawn at 200 km intervals.

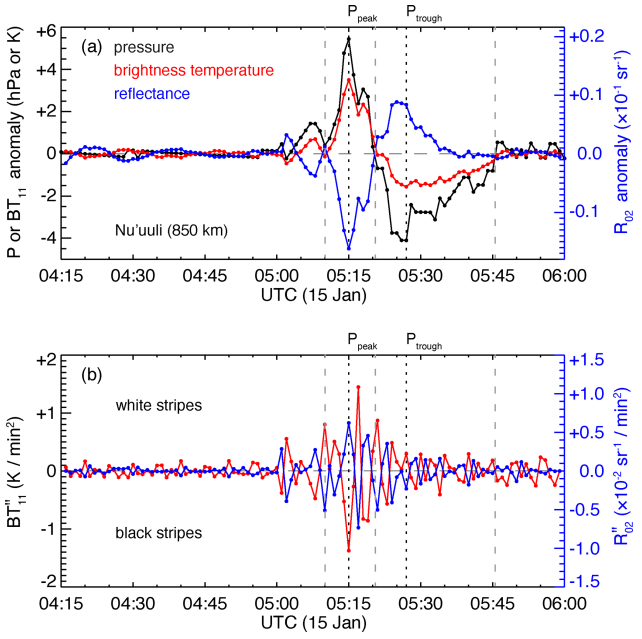

Figure 8. **(a)** Pressure anomalies for Nu'uuli and mean BT_{11} and R_{02} anomalies for the blue domain in Fig. 7, calculated at 1 min resolution on 15 January. **(b)** Second time derivatives BT_{11}'' and R_{02}''. Dotted black lines mark the main pressure peak and pressure trough, P_{peak} and P_{trough}, and dashed gray lines mark the zero-crossings.

period covered in Supplement Animation 1. The northeastward propagation of the waves is obvious in both channels. However, the pattern of alternating black and white stripes is inverted between the infrared and solar reflectance channels at every time step: wherever $BT_{11}'' < 0$, $R_{02}'' > 0$ and vice versa. Figure 7 gives snapshots for 05:15 UTC, when the primary pressure peak of the L1 waveform reached Nu'uuli (Fig. 2). The signs of the second derivatives are clearly opposite. For example, along the 850 km isodistant arc corresponding to the location of Nu'uuli, BT_{11}'' is negative (black), while R_{02}'' is positive (white). This indicates a relative (one time step to the next) warming in brightness temperature and a relative darkening in cloud brightness. Also note that at this point, wave propagation is still mostly isotropic with the wavefront exhibiting only minor deviations from the isodistants.

For a quantitative analysis, Fig. 8 plots the Nu'uuli pressure anomalies as well as the mean BT_{11} and R_{02} anomalies for the blue domain marked in Fig. 7 (all anomalies are calculated by subtracting a 5th-order polynomial fit, as described in Sect. 2.1). The blue domain has the same epicentral distance and, thus, the same wave arrival times as Nu'uuli but contains a considerable amount of low-level liquid clouds underneath thin cirrus, while the area around Nu'uuli is mostly covered by thick convective clouds (see Supplement Animation 1). Therefore, Lamb wave cloud effects are particularly well-pronounced in the blue domain, as indicated by the large second derivatives (Fig. 7c and d).

The mean BT_{11} anomalies show a strong positive correlation with and have the same sign as the pressure anomalies. The main pressure peak and trough lead to brightness temperature anomalies of $+3.5$ and -1.6 K, respectively. Note that the BT_{11} anomalies are an indirect, amplified measure of the actual adiabatic temperature anomalies of $+0.5$ and -0.4 K (~ 0.1 K hPa^{-1}), because the domain-mean BT measures the varying contribution of the warm ocean surface as modulated by the varying cloud amount–reduced cloudiness increases the ocean contribution to the mean and vice versa (Horváth et al., 2025). Reflecting the asymmetry between the positive and negative pressure phases, the warming dominates the cooling. The correlation between the pressure and BT_{11} anomalies is only -0.20 before the $\sim$04:55 UTC arrival of the wave packet but jumps to 0.95 during the passage of the wave.

In contrast, the reflectance anomalies are essentially a mirror image of the pressure anomalies. The pressure and R_{02} anomalies are practically uncorrelated with a coefficient of 0.06 before 04:55 UTC but become strongly anticorrelated with a coefficient of -0.90 during the passage of the wave. The main pressure peak and trough cause domain-mean reflectance anomalies of -6.2 % (darkening) and $+4.0$ % (brightening), respectively. Darkening is more pronounced

than brightening due to the asymmetry between the magnitudes of compression and rarefaction.

Remarkably, the BT_{11} and R_{02} anomalies trace even the fine structure of the pressure anomaly time series. For example, the small local pressure maximum at 05:18 UTC manifests as a local maximum in BT_{11} and as a local minimum in R_{02}. This indicates that brightness temperature and reflectance adjust to pressure changes on a timescale as short as 1 min. In fact, the ground-based video footage confirms that the adjustment occurs even faster, on a timescale of a few seconds (Fig. 5). Such rapid adjustments are possible because the mixing and evaporation timescales that govern the evolution of the cloud droplet size distribution vary between 2–20 s (Tölle and Krueger, 2014).

To elucidate the emergence of the wave patterns seen in Fig. 7c and d, we plot the time variations of BT_{11}'' and R_{02}'' in Fig. 8b. Before the wave arrives, the brightness temperature and reflectance accelerations from unperturbed cloud development are small. The accelerations increase by a factor of 5–10 during the passage of the main pulse and even in the trailing phase (after 05:45 UTC) they are twice as large. The detection of the Lamb wave against the natural background is made possible precisely by (i) the increased magnitude and (ii) the spatial coherence of the second derivative signal. Because the BT_{11} and R_{02} anomalies are of opposite sign – the curves are reflected across the time axis – their second derivatives are also of opposite sign. This is what leads to the inverted patterns of black and white stripes when BT_{11}'' and R_{02}'' are visualized. As the magnitude of the second derivatives diminishes with propagation distance, it becomes increasingly difficult to distinguish the Lamb wave from the background in individual (static) images. Nevertheless, even a weak Lamb wave can be discerned in an animation thanks to the spatially coherent movement of the perturbations.

Note that the BT anomaly is positive and the R anomaly is negative between the first two zero-crossings (compression phase) and the opposite is true between the second and third zero-crossings (rarefaction phase). However, the second derivatives switch signs several times between the zero-crossings, demonstrating that the second derivative alone is indicative of the concavity, not of the sign of the anomaly.

3.3 Far field

We tracked the Lamb wave's propagation beyond American Samoa in full disk and CONUS geostationary imagery. Supplement Animation 3 shows second derivative images covering two complete circuits of the wave in three days, from 03:30 UTC on 15 January to 03:30 UTC on 18 January. We selected channels which, in our experience, give the visually clearest Lamb signal: one of the WV bands for brightness temperature and one of the particle size bands for solar reflectance. Specifically, channels 9 and 6 (6.9 and 2.2 µm) for GOES-17, channels 8 and 6 (6.2 and 2.2 µm) for GOES-16, channels 6 and 3 (7.3 and 1.6 µm) for MSG, and channels 8 and 6 (6.3 and 1.6 µm) for GK2A. The signs of the second derivatives, that is, the signs of the BT and R anomalies, remain inverted during the entire 3 d period. Below, we plot daytime snapshots of the L1 (1st minor-arc), L2 (1st major-arc), L3 (2nd minor-arc), and L4 (2nd major-arc) waves as examples.

3.3.1 GOES-16, 15 January, L1

Figure 9 depicts the L1 wave at 15:00 UTC on 15 January, ∼ 12 000 km from Hunga. Horváth et al. (2025) analyzed the CONUS subset of this wavefront located in the Caribbean. As shown, the transient decrease in cloud reflectance is detectable across the entire Earth disk wherever low-level liquid clouds are present, including the South Atlantic. The cloud darkening is strongest in the Amazon region rather than in the Caribbean featured in Horváth et al. (2025).

At this epicentral distance, deviations from isotropic propagation are already visible. The average propagation speed of the wavefront is higher in Canada and the Southern Ocean than in South America. This is caused primarily by the accumulated effect of global winds, but topography also plays a noticeable role (Sepúlveda et al., 2023). The reflection from the Andes is apparent in Supplement Animation 3 (between 14:00–18:00 UTC on 15 January), especially in the brightness temperature imagery. In fact, the wave undergoes a double reflection as it reaches the Peruvian Andes first and the Chilean Andes slightly later. The east-to-west propagating reflected waves then create weaker but complex interference patterns.

Also note the sunglint at the eastern edge of the wavefront, manifesting as a black–white dipole in the reflectance second derivatives, with the black area (negative concavity) corresponding to a local brightness maximum due to specular reflection. In this case, the sunglint is likely the result of reflection from oriented ice crystals rather than from a water surface. A sharp surface glint from the extensive Amazonian river and lake network is plainly visible in clear areas in channel 2 images. However, this glint signature appears in the 1.37 µm channel 4 "cirrus" band as well, despite surface glint generally missing in channel 4 due to strong water vapor absorption. This indicates that the sunglint in Fig. 9 is caused by a cirrus patch present at this location. Cloud glint caused by horizontally oriented ice crystals is frequently observed by the Earth Polychromatic Imaging Camera (EPIC) onboard the Deep Space Climate Observatory (DSCOVR) located ∼ 1.5 million km from Earth at the Earth–Sun L1 Lagrange point (Várnai et al., 2026). To our knowledge, however, cloud glint has not previously been confidently identified in geostationary imagery.

3.3.2 MSG, 15 January, L1

Figure 10 depicts the L1 wave at 17:15 UTC on 15 January, ∼ 14 000 km from Hunga, with the daytime portion of the

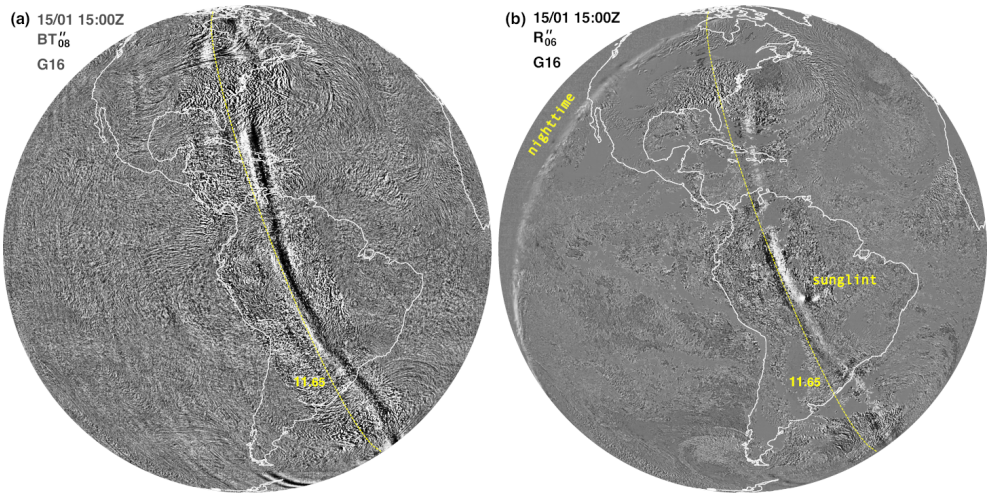

Figure 9. GOES-16 full-disk image of **(a)** BT_{08}'' and **(b)** R_{06}'' at 15:00 UTC on 15 January 2022. The second time derivatives are calculated for $\Delta t = 10$ min. The yellow line of 11 650 km travel distance is plotted as a guide.

wavefront arcing from the North Atlantic to the South Atlantic. As before, the dominant cloud darkening associated with the pressure and temperature increase, and the weaker cloud brightening corresponding to the subsequent pressure and temperature decrease are apparent. As the wave approaches the antipode from different azimuths, the initially concentric wavefronts are distorted into an angular shape by global winds. Also note the sunglint from the ocean surface near the Brazilian coast, which is significantly larger than the cloud glint in the Amazon (Fig. 9).

3.3.3 GK2A, 16 January, L2

Figure 11 shows a snapshot of the L2 wave at 05:50 UTC on 16 January, after a ∼ 29 000 km propagation and first passage through the antipode. In the brightness temperature image, the wavefront stretches from the Russian Arctic to the southern Indian Ocean. The oceanic half of the wavefront, between the Bay of Bengal and the southern Indian Ocean, is clearly detectable in the reflectance image as well, thanks to the presence of low-level clouds. The second derivative patterns and, thus, the temperature and reflectance anomalies remain inverted. In the reflectance channel, the Lamb signal is missing over land due to the lack of liquid clouds or the dominance of glaciated clouds, but a weak ocean glint is present.

3.3.4 GOES-16 and GOES-17, 16 January, L3

Figure 12 presents GOES-16 and GOES-17 snapshots of the L3 wave at 21:30 UTC on 16 January, after a ∼ 46 000 km propagation and two caustic crossings (antipode–epicenter). The wavefront shows considerable distortions from a circle and has an angular shape with sharp corners. The signal is strongest along the meridionally oriented branch running from north-northwest to south-southeast. The GOES-17 images capture a faint signal along the more zonally oriented branch running from west-southwest to east-northeast in the top left segment of the full disk (also see Supplement Animation 3).

The signs of BT″ and R″ are again inverted, indicating opposite brightness temperature and reflectance anomalies. However, the 180° polar phase shift caused by the two caustic crossings effectively inverts the polarity of the anomalies. The dominant (broadest) BT″ signal is positive (white) and the dominant R″ signal is negative (black) for the L3 passage, while the opposite is true for the initial L1 passage (cf. Figs. 9 and 10). Due to the complete phase inversion, the dominant L3 anomalies are the rarefaction and the corresponding cooling and cloud brightening.

3.3.5 GOES-16 CONUS, Santa Barbara, 17 January, L4

As our final example, Fig. 13 depicts GOES-16 CONUS snapshots of the L4 wave at 21:01 UTC on 17 January, after a ∼ 72 000 km propagation and three caustic crossings (antipode–epicenter–antipode). The full disk Lamb signal is shown in Supplement Animation 3. Here, we plot BT″ and R″ near the California coast along the western boundary of the CONUS domain (Fig. 1), exploiting the 5 min cadence of the CONUS scans, which increases signal strength compared to the 10 min FD scans. The presence of low-level clouds, typical in the California stratocumulus region, allows the detection of the Lamb wave in the solar reflectance channel.

The wave patterns are more complex than seen in previous FD plots, partly because the 5 min CONUS images capture higher frequency fluctuations and partly because the L4 waveform is characterized by a small peak followed by a trough–peak–trough sequence, as discussed in Sect. 2.1. Dispersion, distortion due to accumulated wind effects, and

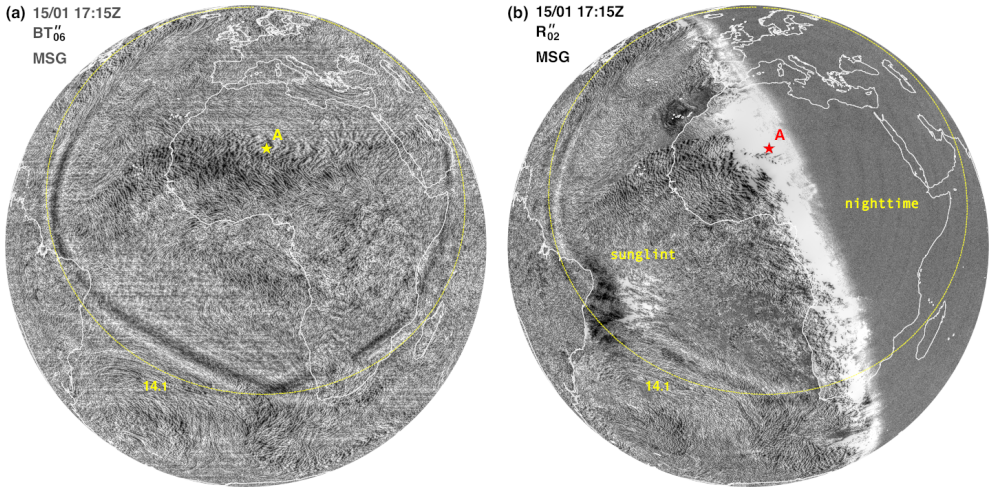

Figure 10. MSG (Meteosat-11) full-disk image of **(a)** BT_{06}'' and **(b)** R_{02}'' at 17:15 UTC on 15 January 2022. The second time derivatives are calculated for $\Delta t = 15$ min. The yellow line of 14 100 km travel distance is plotted as a guide. The star is Hunga's antipode (A).

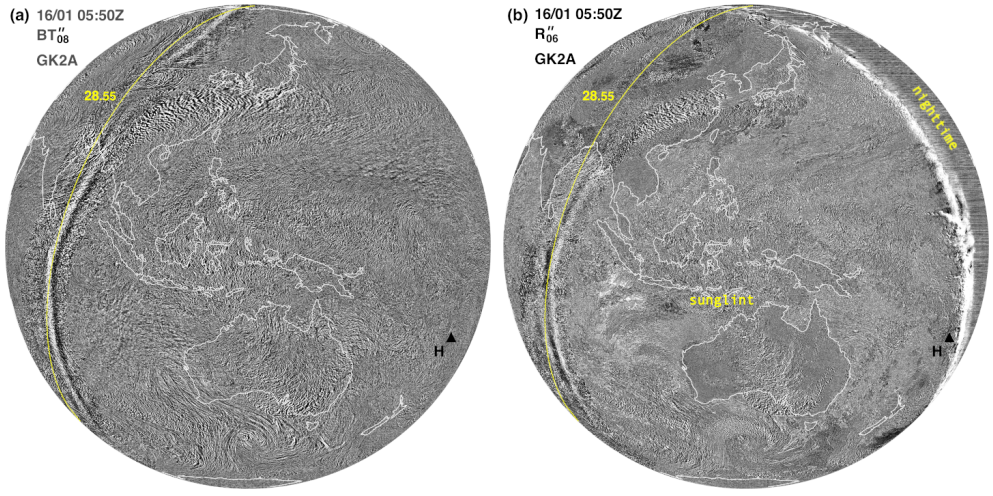

Figure 11. GK2A full-disk image of **(a)** BT_{08}'' and **(b)** R_{06}'' at 05:50 UTC on 16 January 2022. The second time derivatives are calculated for $\Delta t = 10$ min. The yellow line of 28 550 km travel distance is plotted as a guide. The black triangle is Hunga (H).

wave interference also increase complexity. Nevertheless, the BT″ and R″ patterns remain inverted even after a propagation of nearly two full circuits around the globe.

For a quantitative analysis, we selected the yellow domain immediately southwest of Santa Barbara, where the signal is strong in both channels. Figure 14 plots the Santa Barbara pressure anomalies as well as the domain-mean BT_{11} and R_{02} anomalies (all anomalies are calculated by subtracting a 35 min running average). To match the temporal resolution of the CONUS observations, we also show the 5 min pressure anomalies alongside the original 1 min ASOS pressure data.

Similar to the Nu'uuli results (Fig. 8), the brightness temperature anomalies are positively correlated with the pressure anomalies, but the magnitude of the anomalies decreased by a factor of 5–10. The 5 min pressure peak (+0.55 hPa) leads to a BT increase of +0.3 K, while the leading and trailing pressure troughs (−0.27 hPa), occurring 15 min before and after the peak, result in a BT decrease of −0.3 and −0.1 K, respectively. The reflectance anomalies are negatively correlated with the pressure anomalies and are essentially a mirror image of the BT anomalies. The warming and cooling associated with the pressure peak and troughs introduce a relative cloud darkening of −2.1 % and cloud brightening of +1.3 %, respectively, which are approximately a third of the relative reflectance variations observed at Nu'uuli (−6.2 % darkening and +4.0 % brightening).

The 5 min brightness temperature and reflectance accelerations are at least a factor of 20 smaller than the 1 min accelerations at Nu'uuli; nevertheless, they are still detectable against the natural background. The BT″ and R″ are the

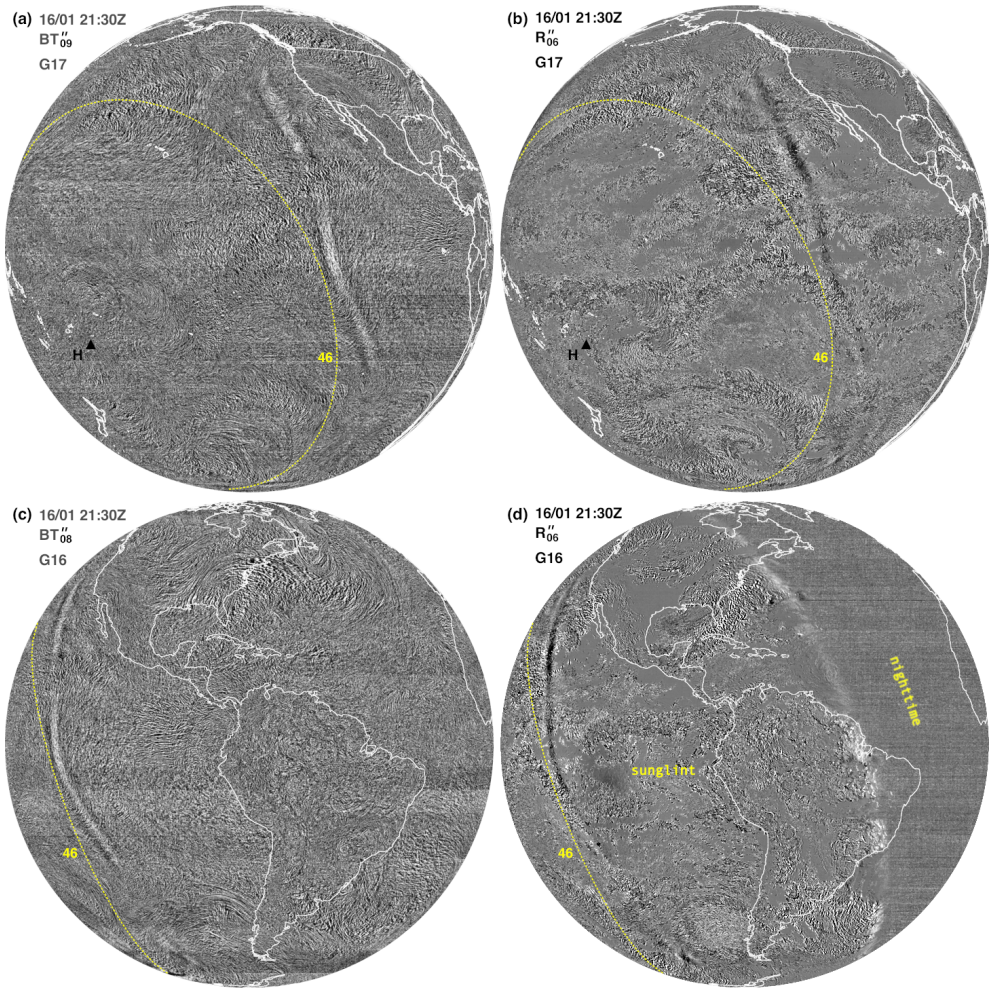

Figure 12. Full-disk images of **(a)** GOES-17 BT_{09}'', **(b)** GOES-17 R_{06}'', **(c)** GOES-16 BT_{08}'', and **(d)** GOES-16 R_{06}'' at 21:30 UTC on 16 January 2022. The second time derivatives are calculated for $\Delta t = 10$ min. The yellow line of 46 000 km travel distance is plotted as a guide. The black triangle is Hunga (H).

largest during the passage of the pressure peak and show higher-frequency variations in the trailing phase than in the leading phase. They are consistently of opposite sign, causing the inverted patterns in Fig. 13.

4 Discussion and summary

We investigated the global effects of the 2022 Hunga Lamb wave on meteorological clouds over a multi-day period, expanding upon the spatiotemporally limited study of Horváth et al. (2025) by combining ground-based video footage, surface pressure records, and geostationary satellite imagery. Satellite observations revealed that within ∼ 400–500 km of the eruption, the compressional warming phase of the wave evaporated low-level clouds, while the subsequent rarefactional cooling phase led to the condensation of liquid clouds, which dissipated in ∼ 15 min as pressure and temperature recovered. The Nuku'alofa video (∼ 73 km from Hunga) clearly showed evaporation–condensation cycles in low-level clouds with a period as short as ∼ 40 s, not only due to the primary pressure pulse but also the weaker precursor pulses.

At greater propagation distances, the wave amplitude was insufficient to trigger substantial cloud formation in clear areas. Nevertheless, the wave-induced temperature and relative humidity fluctuations caused reflectance fluctuations in preexisting clouds, which were detectable in satellite observations over long travel paths. This behavior is demonstrated by the consistently opposite signs of the brightness temperature and reflectance second derivatives, leading to inverted black–white striped patterns in BT″ and R″ images (Supplement Animation 3). The satellite observations were quantitatively evaluated against surface pressure records at Nu'uuli on 15 January and Santa Barbara on 17 January, corresponding to propagation distances of ∼ 850 and ∼ 72 000 km, respectively. The Lamb wave's compression and rarefaction anomalies drove highly correlated warming and cooling

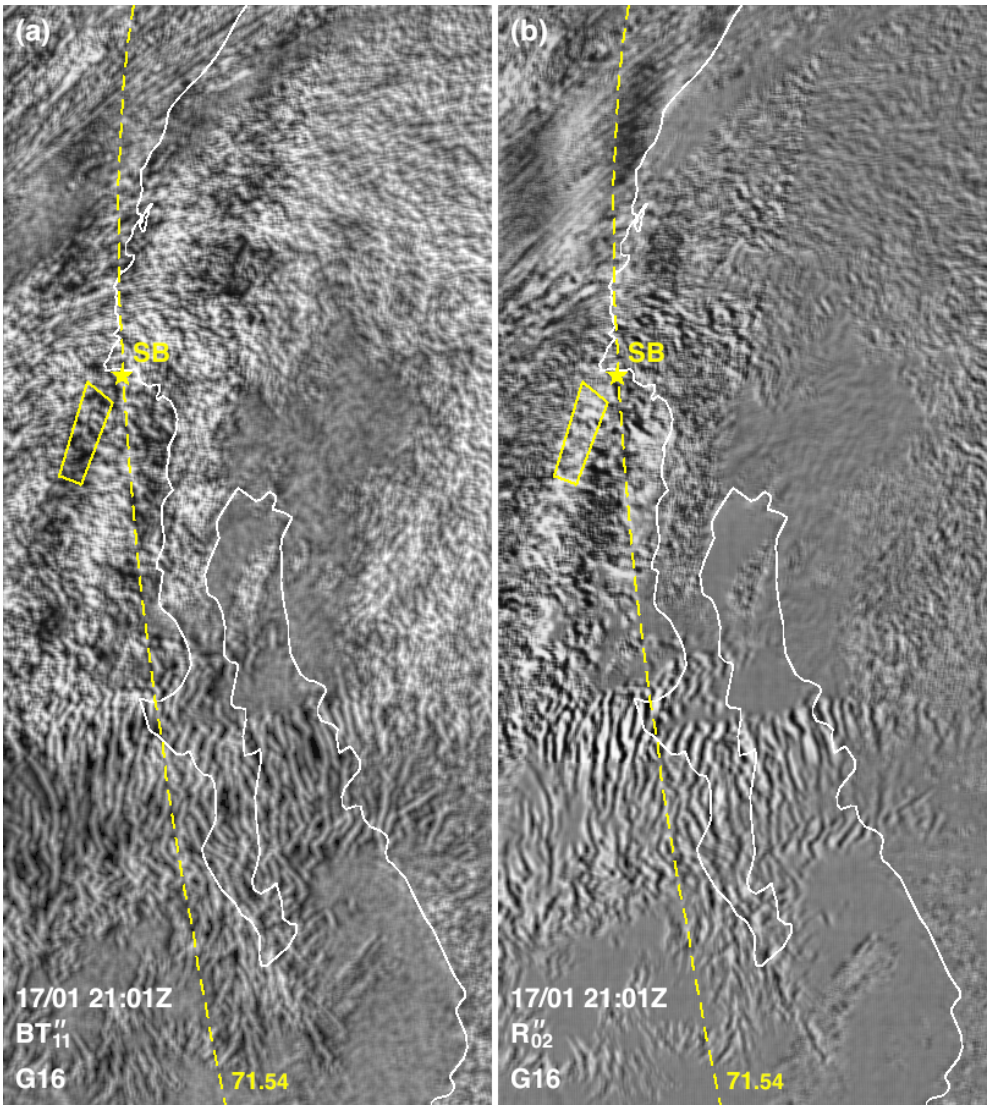

Figure 13. GOES-16 CONUS image of **(a)** BT_{11}'' and **(b)** R_{02}'' at 21:01 UTC on 17 January 2022. The second time derivatives are calculated for $\Delta t = 5$ min. The yellow line of 71,540 km travel distance is plotted as a guide. The yellow star is Santa Barbara (SB). The yellow domain is the cloudy area analyzed in Fig. 14.

anomalies, which in turn caused darkening and brightening reflectance signatures. Cloud reflectance followed temperature variations almost instantaneously, because the mixing and evaporation timescales governing the evolution of the droplet size distribution are on the order of seconds. The magnitude of reflectance anomalies reached 6 % at Nu'uuli and persisted at 2 % at Santa Barbara, even after 2.5 d of global propagation.

The relative strengths of warming–cooling and their corresponding darkening–brightening anomalies varied as the waveform underwent a 90° phase shift upon each caustic crossing. During the L1 minor-arc passage, warming and darkening were dominant because compression was higher in magnitude than rarefaction in the initial Lamb wave. In contrast, cooling and brightening dominated during the L3 minor-arc passage, as the wave polarity inverted due to a cumulative 180° phase shift across two caustic crossings.

A fundamental question is the atmospheric residence time of the Lamb wave. To estimate the lifetime of the Hunga Lamb wave, Supplement Animations 4 and 5 show the GOES-16 BT_{08}'' and R_{06}'', respectively, for a ∼ 10 d period from 03:30 UTC on 15 January to 23:40 UTC on 24 January. Animating the second derivative images (especially at double video playback speed), helps the visual detection even of faint signals due to the spatially coherent movement of the wavefront. In the water vapor BT_{08}'', we could identify ∼ 12 passages in the 8 d up to 23 January (minor-arc L1–L11 and major-arc L2–L12), corresponding to ∼ 6 full circuits around

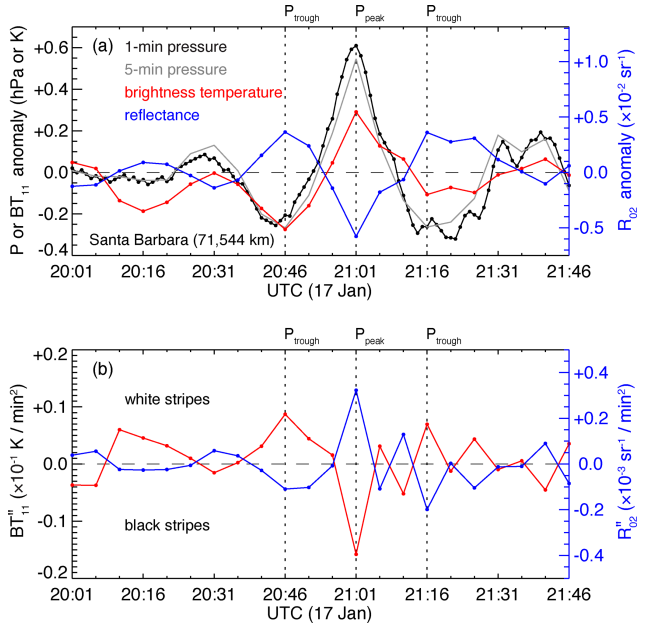

Figure 14. **(a)** Pressure anomalies for Santa Barbara and mean BT_{11} and R_{02} anomalies for the yellow domain in Fig. 13, calculated at 5 min resolution on 17 January. **(b)** Second time derivatives BT_{11}'' and R_{02}''. Dotted black lines mark the 5 min pressure peak and pressure troughs, P_{peak} and P_{trough}.

the Earth or a total propagation distance of ∼ 240 000 km. In the daytime reflectance R_{06}'', where the signal is weaker, we could identify ∼ 9 passages in the 6 d up to 21 January (L1–L9, and L4 and L8; L2 and L6 occurred during nighttime), corresponding to ∼ 4 full circuits or a total travel distance of ∼ 160 000 km.

By comparison, foundational studies of previous large explosions had to rely exclusively on surface pressure data to track the Lamb wave. For the 1883 Krakatoa eruption, seven wave passages were detected (L1–L7 and L2–L6) in ∼ 5 d, equal to 3–4 full circuits (Gabrielson, 2010; Symons, 1888). For the 1961 Tsar Bomba, 5 wave passages (L1–L5 and L2–L4) or ∼ 2 full circuits were observed in ∼ 3 d (Carpenter et al., 1961; Donn and Ewing, 1962). For the 1991 Pinatubo eruption, on the other hand, only 3 passages (L1–L3 and L2) or 1–2 full circuits were reliably identified in ∼ 2 d (Tahira et al., 1996). Note, however, that the 1883 Krakatoa eruption was comprehensively investigated by the Royal Society, while the pressure waves generated by the other two explosions received less scientific attention. In addition, the longer duration ($\gtrsim$ 2 h) and lower intensity of the 1991 Pinatubo explosion make its Lamb waves more difficult to detect than those from the impulsive Hunga source (Watada and Kanamori, 2010). Regardless, the record wave passages detected from the Hunga eruption clearly demonstrate the vastly improved capabilities of the modern global monitoring networks, particularly satellite observations.

Finally, the observed lifetime of the Hunga Lamb wave conforms remarkably well to early theoretical studies. Lindzen and Blake (1972) investigated the lifetime of Lamb waves in an atmosphere with realistic temperature distributions and dissipation. For a wave with a period of 1 h – the shortest period considered and closest to the 30–50 min period of the Hunga wave – they calculated a lifetime of ∼ 7 d or ∼ 168 wave cycles, governed primarily by the dissipative time scale of surface friction. At the upper bound of the reported periods (50 min), the Hunga Lamb wave completes approximately 230 cycles during its 8 d lifetime, aligning well with the theoretical estimate.

Appendix A: Blast-to-Lamb wave kinematics

As the shock wave diminishes with distance, the peak overpressure falls toward values comparable to ambient atmospheric conditions and the disturbance transitions into the acoustic regime. Beyond this point, the wave speed approaches the local speed of sound, and further evolution is mostly controlled by the vertical structure of the atmosphere. Several wave types can be simultaneously supported in the atmosphere, including internal acoustic-gravity waves that propagate diagonally and lose energy to upward radiation, and a small set of resonant or transient modes confined near the surface. Among the latter, the Lamb wave (Lamb, 1932) is an exact solution of the linearized hydrodynamic equations for a compressible, layered atmosphere bounded below by a rigid surface. Its horizontal propagation implies that the disturbance does not radiate energy upward and the amplitude decays exponentially with height while persisting in its horizontal motion. Analyzing barograph records from the 1883 Krakatoa eruption, Pekeris (1939, 1948) showed that this mode could account for pressure pulses recorded at global distances and identified its phase speed as closely matching the surface speed of sound, near 308–318 m s^{-1} depending on local temperature.

The mechanism by which a 3D blast wave feeds energy into this 2D surface mode involves partial mode conversion during outward propagation. As the spherical front expands, components of the disturbance with steep vertical wavenumbers continue upward into the upper atmosphere, where some of the energy is permanently lost. The portion of energy with a near-horizontal wavenumber, however, satisfies the dispersion relation of the Lamb mode and is retained at the surface indefinitely, since it has no vertical group velocity to carry it away. Over distances of several hundred to a few thousand kilometers, this filtering process leaves the fundamental Lamb mode as the dominant surviving signal, increasingly distinguishable from the broader spectrum of acoustic-gravity arrivals that disperse, attenuate, or radiate vertically.

The persistence of the Lamb mode is also reinforced by its geometric spreading. The near-field shock loses amplitude through both spherical spreading ($1/r$) and nonlinear dissi-

pation, whereas the energy of the far-field Lamb wave is confined in the troposphere and spreads only cylindrically; thus, its amplitude decays as $1/\sqrt{r}$ (Pekeris, 1948; Bretherton, 1969). This weaker geometric attenuation, combined with the absence of vertical radiation loss, allows the Lamb wave to remain detectable at planetary distances long after the decay of the original shock wave.

The 2022 Hunga eruption provided a well-instrumented modern record of the resulting Lamb wave, although the 3D to 2D conversion process itself was not directly resolved by the available sensor network. Global barometric networks recorded a Lamb wave signal that circled the Earth multiple times over several days, with a phase speed consistent with the classical Pekeris value (Díaz and Rigby, 2022b; Wright et al., 2022; Matoza et al., 2022). Many media accounts of the Hunga eruption described the global pressure pulse as a "shock wave" circling the planet, a characterization that misidentifies two physically distinct phenomena. A genuine shock wave did form at the vent, but its supersonic, high-overpressure character was short-lived: within a few kilometers the nonlinear disturbance decayed and relaxed into a linear acoustic wave, consistent with the rapid attenuation expected of finite-amplitude blast waves (Reed, 1972; Kinney and Graham, 1985).

An estimate of the beginning of the shock-decay distance can be directly obtained from an analytical approximation of the Mach number of the shock front M_S (Díaz and Rigby, 2022a):

$$M_S(z) = \left(1 + \frac{1}{K_0 z^3}\right)^{1/2}, \tag{A1}$$

where the dimensionless length z is given in terms of the radius of the spherical wave R, the energy released E_0, and the unperturbed atmospheric pressure P_0 as $z = R(P_0/E_0)^{1/3}$. The constant $K_0 = 7.46$ arises from the solution of the hydrodynamic equations describing the pressure, density, and speed of the gas enclosed by the shock front. Equation (A1) shows that the acoustic regime dominates when

$$R \gtrsim \left(\frac{E_0}{P_0 K_0}\right)^{1/3}. \tag{A2}$$

Considering Hunga's estimated energy release of 61–200 Mt (Adushkin et al., 2022; Díaz and Rigby, 2022b), accounting for the energy dissipation in the form of large water displacements (Coleman et al., 1954), and using an average atmospheric pressure of 1000 hPa, Eq. (A2) yields $R \gtrsim 8.2$–12.2 km. This shows that beyond ~ 10 km from the vent, the shock wave transitioned into a linear acoustic wave and that this is what was observed at the closest documented observation point in Nuku'alofa, located ~ 73 km away. Barograph networks, microbarometers, and satellite imagery subsequently tracked waves across the globe over several days, including multiple circumnavigations; nonetheless, this was not the initial shock wave but the atmospheric Lamb mode, propagating at a nearly constant phase speed close to the surface speed of sound and showing none of the steep-fronted, supersonic signature characteristic of a true shock (Díaz and Rigby, 2022b; Matoza et al., 2022; Wright et al., 2022). Satellite observations of concentric brightness temperature anomaly rings expanding from Tonga, widely captioned in the press as a "shock wave" traversing the atmosphere, were in fact imaging this same surface-trapped Lamb disturbance, whose horizontal cylindrical spreading and lack of vertical radiation are properties specific to the linear Lamb mode rather than to shock propagation. The terminological imprecision is understandable given the striking satellite footage, but it obscures the underlying physics: the far-traveling signal was a guided acoustic mode, not a shock wave.

Code availability. The open-source Fiji image processing package is available from the project website at https://imagej.net/software/fiji (last access: 4 July 2026). The software is permanently archived and citable via https://doi.org/10.1038/nmeth.2019 (Schindelin et al., 2012).

Data availability. GOES-R Series Advanced Baseline Imager (ABI) Level 1b Radiances were obtained from the National Oceanic and Atmospheric Administration (NOAA) National Centers for Environmental Information at https://doi.org/10.7289/V5BV7DSR (GOES-R, 2017). The High Rate SEVIRI Level 1.5 Image Data – MSG – 0 degree satellite data were obtained from the European Organisation for the Exploitation of Meteorological Satellites (EUMETSAT) Data Store. The data are publicly accessible under Product ID EO:EUM:DAT:MSG:HRSEVIRI (https://data.eumetsat.int/product/EO:EUM:DAT:MSG:HRSEVIRI; EUMETSAT, 2009). The Geo-KOMPSAT-2A (GK2A) Advanced Meteorological Imager (AMI) satellite data were obtained from the Korea Meteorological Administration (KMA) Weather Data Open Portal (https://data.kma.go.kr/data/rmt/rmtList.do?code=21&pgmNo=683; Korea Meteorological Administration, 2019). The Santa Barbara Municipal Airport (station identifier KSBA) Automated Surface Observing System (ASOS) 1 min Page 2 surface pressure data were obtained from the NOAA National Centers for Environmental Information (NCEI) archive (https://www.ncei.noaa.gov/access/metadata/landing-page/bin/iso?id=gov.noaa.ncdc:C00387; NOAA, 2005).

The Coconut Point, American Samoa surface pressure data and the Supplement Animations referenced in the text are available at https://doi.org/10.5281/zenodo.20591199 (Horváth et al., 2026).

Author contributions. ÁH developed the idea and methodology and performed the analysis with contributions from JD and SR. ÁH prepared the manuscript with significant contributions from all authors.

Competing interests. The contact author has declared that none of the authors has any competing interests.

Disclaimer. Publisher's note: Copernicus Publications remains neutral with regard to jurisdictional claims made in the text, published maps, institutional affiliations, or any other geographical representation in this paper. The authors bear the ultimate responsibility for providing appropriate place names. Views expressed in the text are those of the authors and do not necessarily reflect the views of the publisher.

Acknowledgements. Ákos Horváth is supported by the German Research Foundation project "*Understanding volcanogenic gravity waves by synergistic use of modelling and observations*". This study also contributes to the Cluster of Excellence "CLICCS II – Climate, Climatic Change, and Society", and to the Earth and Society Research Hub (ESRAH) of the University of Hamburg. We thank Joe LaPlante (joseph.laplante@noaa.gov) for providing the Coconut Point, American Samoa surface pressure data from his personal weather station and Brendon M. MacDonald (@MolisiDelmar) for his permission to use the Nuku'alofa video footage, freely available on YouTube. The suggestions of Shingo Watada, The University of Tokyo, Japan and an anonymous reviewer greatly improved the paper.

Financial support. This research has been supported by the Deutsche Forschungsgemeinschaft (grant no. 572704081).

The article processing charges for this open-access publication were covered by the Karlsruhe Institute of Technology (KIT).

Review statement. This paper was edited by Matthew Christensen and reviewed by Shingo Watada and one anonymous referee.

References

Abyssius (@abyssius2838): Volcano Eruption in Papua New Guinea, YouTube [video], available at: https://youtu.be/BUREX8aFbMs (last access: 4 July 2026), 2014.

Adushkin, V. V., Rybnov, Y. S., and Spivak A. A.: Geophysical effects of the eruption of Hunga-Tonga-Hunga-Ha'apai Volcano on January 15, 2022, Dokl. Earth Sci., 504, 362–367, https://doi.org/10.1134/s1028334X22060034, 2022.

afarTV (@afartv): Nov 24, 2025: Lava, Shockwave, Pyroclastic Flow at Fuego Volcano, Guatemala, YouTube [video], available at: https://youtu.be/eRJOIzZg78o (last access: 4 July 2026), 2025.

APARC: The Hunga Volcanic Eruption Atmospheric Impacts Report, edited by: Yunqian Z., Mann, G., Newman, P. A., and Randel, W., APARC Report No. 11, WCRP Report No. 10/2025, https://doi.org/10.34734/FZJ-2025-05237, https://aparc-climate.org/publications/aparc-report-no-11/ (last access: 18 November 2026), 2025.

ArchiveRandom (@ArhiveRandom): Volcanic Shockwave from Mt. Dukono in Indonesia, YouTube [video], https://youtube.com/watch?v=Eru3_hf61RY (last access: 4 July 2026), 2025.

ASOS: Index of /data/automated-surface-observing-system-one-minute-pg2/, National Centers for Environmental Information (NCEI), https://www.ncei.noaa.gov/access/search/datasets/auto-surf-obs-sys-1-min-pg2/ (last access: 18 November 2026),

atomcentral (@atomcentral): Crossroads Baker, YouTube [video], https://youtu.be/gy6-ZKWCoH0 (last access: 4 July 2026), 2016.

Barnaboule69: Very rare video of the ash plume from the 2022 Hunga Tonga eruption seen at ocean level, Reddit/ r/Volcanoes [video], https://www.reddit.com/r/Volcanoes/s/iJXM6U60MG (last access: 4 July 2026), 2022.

Bonner, J., Waxler, R., Gitterman, Y., and Hofstetter, R.: Seismo-acoustic energy partitioning at near-source and local distances from the 2011 Sayarim explosions in the Negev Desert, Israel, Bull. Seismol. Soc. Am., 103, 741–758, https://doi.org/10.1785/0120120181, 2013.

Bretherton, F. P.: Lamb waves in a nearly isothermal atmosphere, Q. J. R. Meteorol. Soc, 95, 754–757, https://doi.org/10.1002/qj.49709540608, 1969.

Britannica Editors: Krakatoa | Volcano, Geology, Eruptions, & Anak Krakatau | Britannica, Encyclopedia Britannica, https://www.britannica.com/place/Krakatoa (last access: 4 July 2026), 2026.

Brune, J. N., Nafe, J. E., and Alsop, L. E.: The polar phase shift of surface waves on a sphere, Bull. Seismol. Soc. Am., 51, 247–257, https://doi.org/10.1785/BSSA0510020247, 1961.

Carpenter, E., Harwood, G., and Whiteside, T.: Microbarograph records from the Russian large nuclear explosions, Nature, 192, 857, https://doi.org/10.1038/192857a0, 1961.

Carr, J. L., Horváth, Á., Wu, D. L., and Friberg, M. D.: Stereo plume height and motion retrievals for the record-setting Hunga Tonga-Hunga Ha'apai eruption of 15 January 2022, Geophys. Res. Lett., 49, e2022GL098131, https://doi.org/10.1029/2022GL098131, 2022.

Chen, H., Zhang, D., Carton, J., and Atlas, R.: On the rapid intensification of Hurricane Wilma (2005). Part I: Model prediction and structural changes, Wea. Forecasting, 26, 885–901, https://doi.org/10.1175/WAF-D-11-00001.1, 2011.

Coleman, K. D., Project Officers, and Commanders of Task Units: Operation CASTLE. Summary Report of the Commander, Task Unit 13. Military Effects, Programs 1–9, Defense Technical Information Center (DTIC), Report No. WT-934 / Accession ID: ADA995123, https://rminucleardocs.icaad.ngo/en/entity/njum5hp2op/ (last access: 4 July 2026), 1954.

Czarnecki, A. J., Czarnecki, A., Secrist, R., and Willsey, J.: Shock Wave in the Beirut Explosion: Theory and Video Analysis, arXiv [preprint], https://doi.org/10.48550/arXiv.2510.24742, 2026.

Dalal, P., Kundu, B., Panda, J., and Jin, S.: Atmospheric Lamb wave pulse and volcanic explosivity index following the 2022 Hunga Tonga (South Pacific) eruption, Front. Earth Sci., 10:931545, https://doi.org/10.3389/feart.2022.931545, 2023.

Díaz, J. S.: Explosion analysis from images: Trinity and Beirut, Eur. J. Phys., 42, 035803, https://doi.org/10.1088/1361-6404/abe131, 2021.

Díaz, J. S. and Rigby, S. E.: Blast wave kinematics: theory, experiments, and applications, Shock Waves, 32, 405–415, https://doi.org/10.1007/s00193-022-01089-z, 2022a.

Díaz, J. S. and Rigby, S. E.: Energetic output of the 2022 Hunga Tonga–Hunga Ha'apai volcanic eruption from

pressure measurements, Shock Waves, 32, 553–561, https://doi.org/10.1007/s00193-022-01092-4, 2022b.

Donn, W. L. and Ewing, M.: Atmospheric waves from nuclear explosions – Part II: The Soviet test of 30 October 1961, J. Atmos. Sci., 19, 264–273, https://doi.org/10.1175/1520-0469(1962)019<0264:AWFNEI>2.0.CO;2., 1962.

EUMETSAT: High Rate SEVIRI Level 1.5 Image Data – MSG – 0 degree, ID: EO:EUM:DAT:MSG:HRSEVIRI, EUMETSAT Data Store [data set], https://data.eumetsat.int/product/EO:EUM:DAT:MSG:HRSEVIRI (last access: 4 July 2026), 2009.

Evers, L. G. and Haak, H. W.: Listening to sounds from an exploding meteor and oceanic waves, Geophys. Res. Lett., 28, 4385–4388, https://doi.org/10.1029/2000GL011859, 2001.

Fee, D., Waxler, R., Assink, J., Gitterman, Y., Given, J., Coyne, J., Mialle, P., Garces, M., Drob, D., Kleinert, D., Hofstetter, R., and Grenard, P.: Overview of the 2009 and 2011 Sayarim infrasound calibration experiments, J. Geophys. Res.-Atmos., 118, 6122–6143, https://doi.org/10.1002/jgrd.50398, 2013.

Gabrielson, T. B.: Krakatoa and The Royal Society: The Krakatoa explosion of 1883, Acoustics Today, 6, 14–19, https://acousticstoday.org/issues/2010AT/Apr2010/ (last access: 4 July 2026), 2010.

Garrett, C. J. R.: Atmospheric edge waves, Q. J. R. Meteorol. Soc., 95, 731–753, https://doi.org/10.1002/qj.49709540607, 1969.

Genco, R., Ripepe, M., Marchetti, E., Bonadonna, C., and Biass, S.: Acoustic wavefield and Mach wave radiation of flashing arcs in strombolian explosion measured by image luminance, Geophys. Res. Lett., 41, 7135–7142, https://doi.org/10.1002/2014GL061597, 2014.

GOES-R: GOES-R Calibration Working Group and GOES-R Series Program, NOAA GOES-R Series Advanced Baseline Imager (ABI) Level 1b Radiances [data set], https://doi.org/10.7289/V5BV7DSR, 2017.

Gupta, A. K., Bennartz, R., Fauria, K .E., and Mittal, T.: Eruption chronology of the December 2021 to January 2022 Hunga Tonga-Hunga Ha'apai eruption sequence, Commun. Earth Environ., 3, 314, https://doi.org/10.1038/s43247-022-00606-3, 2022.

Gusman, A. R. and Tanioka, Y.: Atmospheric Lamb wave inversion from the 2022 Hunga Tonga–Hunga Ha'apai eruption for tsunami prediction, Geosci. Lett., 12, 32, https://doi.org/10.1186/s40562-025-00404-7, 2025.

Harding, B. J., Wu, Y.-J. J., Alken, P., Yamazaki, Y., Triplett, C. C., Immel, T. J., Gasque, L. C, Mende, S. B., and Xiong, C.: Impacts of the January 2022 Tonga volcanic eruption on the ionospheric dynamo: ICON-MIGHTI and swarm observations of extreme neutral winds and currents, Geophys. Res. Lett., 49, e2022GL098577, https://doi.org/10.1029/2022GL098577, 2022.

Harkrider, D. and Press, F.: The Krakatoa air-sea waves: An example of pulse propagation in coupled systems, Geophys. J. Int., 13, 149–159, https://doi.org/10.1111/j.1365-246X.1967.tb02150.x, 1967.

Hoarau, K.: Supertyphoon Forrest (September 1983): The overlooked record holder of intensification in 24, 36, and 48 h, Wea. Forecasting, 15, 357–360, https://doi.org/10.1175/1520-0434(2000)015<0357:SFSTOR>2.0.CO;2, 2000.

Holasek, R. E., Self, S., and Woods, A. W.: Satellite observations and interpretation of the 1991 Mount Pinatubo eruption plumes, J. Geophys. Res., 101, 27635–27655, https://doi.org/10.1029/96JB01179, 1996.

Horváth, Á., Vadas, S. L., Stephan, C. C., and Buehler, S. A.: One-minute resolution GOES-R observations of Lamb and gravity waves triggered by the Hunga Tonga-Hunga Ha'apai eruptions on 15 January 2022, J. Geophys. Res.-Atmos., 129, e2023JD039329, https://doi.org/10.1029/2023JD039329, 2024.

Horváth, Á., Adams, D. K., Liu, M., Sepúlveda, I., Sakradzija, M., and Buehler, S. A.: Transient darkening of low-level liquid clouds by the 2022 Hunga Lamb wave observed in GOES-R imagery, Geophys. Res. Lett., 52, e2025GL115935, https://doi.org/10.1029/2025GL115935, 2025.

Horváth, Á., Adams, D. K., Diaz, J. S., Rigby, S., Buehler, S. A., and Sakradzija, M.: Animations, video footage, and Coconut Point pressure data for "Measurement report: Geostationary satellite and ground-based video observations of cloud brightness variations triggered by the 2022 Hunga Lamb wave", Zenodo [video supplement], https://doi.org/10.5281/zenodo.20591199, 2026.

Kinney, G. F. and K. J. Graham: Explosive Shocks in Air, 2nd edn., Springer-Verlag, New York, NY, https://doi.org/10.1007/978-3-642-86682-1, 1985.

Korea Meteorological Administration: Geo-KOMPSAT-2A (GK2A) Advanced Meteorological Imager (AMI) Meteorological Satellite Data, KMA Weather Data Open Portal [data set], https://data.kma.go.kr/data/rmt/rmtList.do?code=21&pgmNo=683 (last access: 4 July 2026), 2019.

Kubota, T., Saito, T., and Nishida, K.: Global fast-traveling tsunamis driven by atmospheric Lamb waves on the 2022 Tonga eruption, Science, 377, 91–94, https://doi.org/10.1126/science.abo4364, 2022.

Lamb, H.: Hydrodynamics, 6th edn., Dover Publications, New York, NY, https://archive.org/details/hydrodynamics00lamb (last access: 4 July 2026), 1932.

Le Pichon, A., Blanc, E., and Hauchecorne, A. (Eds.): Infrasound Monitoring for Atmospheric Studies, 2nd edn., Springer Cham, https://doi.org/10.1007/978-3-319-75140-5, 2019.

Lindzen, R. S. and Blake, D.: Lamb waves in the presence of realistic distributions of temperature and dissipation, J. Geophys. Res., 77, 2166–2176, https://doi.org/10.1029/JC077i012p02166, 1972.

MacDonald, B. M. (@MolisiDelmar): Extended footage – Tongas Jan15th volcanic eruption Hunga Tonga Hunga Ha'apai as seen from the ground, YouTube [video], https://youtu.be/3US-AxvGfE4 (last access: 4 July 2026), 2022.

MacFerrin, M., Amante, C., Carignan, K., Love, M., and Lim, E.: The Earth Topography 2022 (ETOPO 2022) global DEM dataset, Earth Syst. Sci. Data, 17, 1835–1849, https://doi.org/10.5194/essd-17-1835-2025, 2025.

Mastin, L. G., Van Eaton, A. R., and Cronin, S. J.: Did steam boost the height and growth rate of the giant Hunga eruption plume?, Bull. Volcanol., 86, 64, https://doi.org/10.1007/s00445-024-01749-1, 2024.

Matoza, R. S., Fee, D., Assink, J. D., Iezzi, A. M., Green, D. N., Kim, K., Toney, L., Lecocq, T., Krishnamoorthy, S., Lalande, J.-M., Nishida, K., Gee, K. L., Haney, M. M., Ortiz, H. D., Brissaud, Q., Martire, L., Rolland, L., Vergados, P., Nippress, A., Park, J., Shani-Kadmiel, S., Witsil, A., Arrowsmith, S., Caudron, C., Watada, S., Perttu, A. B., Taisne, B., Mialle, P., Le Pichon, A., Vergoz, J., Hupe, P., Blom, P. S., Waxler, R., De Angelis, S., Snively, J. B., Ringler, A. T., Anthony, R. E., Jolly, A. D., Kilgour, G., Averbuch, G., Ripepe, M., Ichi-

hara, M., Arciniega-Ceballos, A., Astafyeva, E., Ceranna, L., Cevuard, S., Che, I.-Y., De Negri, R., Ebeling, C. W., Evers, L. G., Franco-Marin, L. E., Gabrielson, T. B., Hafner, K., Harrison, R. G., Komjathy, A., Lacanna, G., Lyons, J., Macpherson, K. A., Marchetti, E., McKee, K. F., Mellors, R. J., Mendo-Pérez, G., Mikesell, T. D., Munaibari, E., Oyola-Merced, M., Park, I., Pilger, C., Ramos, C., Ruiz, M. C., Sabatini, R., Schwaiger, H. F., Tailpied, D., Talmadge, C., Vidot, J., Webster, J., and Wilson, D. C.: Atmospheric waves and global seismoacoustic observations of the January 2022 Hunga eruption, Tonga, Science, 377, 95–100, https://doi.org/10.1126/science.abo7063, 2022.

McCorkel, J., Van Naarden, J., Lindsey, D., Efremova, B., Coakley, M., Black, M., and Krimchansky, A.: GOES-17 advanced baseline imager performance recovery summary, In Proceedings of IGARSS 2019 – IEEE International Geoscience and Remote Sensing Symposium, https://doi.org/10.1109/igarss40859.2019.9044466, 2019.

McNutt, S. R., Williams, E. R., Spera, F. J., and Scruggs, M. A.: Estimates of condensed water in and energetics of the Hunga volcanic plume on 15 January 2022, Bull. Volcanol., 88, 67, https://doi.org/10.1007/s00445-026-01978-6, 2026.

Millán, L., Santee, M. L., Lambert, A., Livesey, N. J., Werner, F., Schwartz, M. J., Pumphrey, H. C., Manney, G. L., Wang, Y., Su, H., Wu, L., Read, W. G., and Froidevaux, L.: The Hunga Tonga-Hunga Ha'apai hydration of the stratosphere, Geophys. Res. Lett., 49, e2022GL099381, https://doi.org/10.1029/2022GL099381, 2022.

Nairn, I. A.: Atmospheric shock waves and condensation clouds from Ngauruhoe explosive eruptions, Nature, 259, 190–192, https://doi.org/10.1038/259190a0, 1976.

NOAA: NOAA National Weather Service, U.S. Federal Aviation Administration, U.S. Department of Defense, NOAA National Centers for Environmental Information, 1-Minute Page 2 Surface Weather Observations from the Automated Surface Observing Systems (ASOS) Network, NCEI DSI 6406_02 [data set], https://www.ncei.noaa.gov/access/search/datasets/auto-surf-obs-sys-1-min-pg2/ (last access: 4 July 2026), 2005.

Otsuka, S.: Visualizing Lamb waves from a volcanic eruption using meteorological satellite Himawari-8, Geophys. Res. Lett., 49, e2022GL098324, https://doi.org/10.1029/2022GL098324, 2022.

Pekeris, C. L.: Atmospheric oscillations, Proc. R. Soc. Lond. A, 158A, 650–671, https://doi.org/10.1098/rspa.1937.0046, 1937.

Pekeris, C. L.: The propagation of a pulse in the atmosphere, Proc. R. Soc. Lond. A, 171, 434–449, https://doi.org/10.1098/rspa.1939.0076, 1939.

Pekeris, C. L.: The propagation of a pulse in the atmosphere, Part II, Phys. Rev., 73, 145–154, https://doi.org/10.1103/PhysRev.73.145, 1948.

Prata, A. T., Grainger, R. G., Taylor, I. A., and Lambert, A.: Transient ice ring observed during the 15 January 2022 eruption of Hunga volcano, Commun. Earth Environ., 6, 901, https://doi.org/10.1038/s43247-025-02875-0, 2025.

Proud, S. R., Prata, A. T., and Schmauss, S.: The January 2022 eruption of Hunga Tonga-Hunga Ha'apai volcano reached the mesosphere, Science, 378, 554–557, https://doi.org/10.1126/science.abo4076, 2022.

Purkis, S. J., Ward, S. N., Fitzpatrick, N. M., Garvin, J. B., Slayback, D., Cronin, S. J., Palaseanu-Lovejoy, M., and Dempsey, A.: The 2022 Hunga-Tonga megatsunami: Near-field simulation of a once-in-a-century event, Sci. Adv., 9, eadf5493, https://doi.org/10.1126/sciadv.adf5493, 2023.

Reed, J. W.: Air pressure waves from Mount St. Helens eruptions, J. Geophys. Res., 92, 11979–11992, https://doi.org/10.1029/JD092iD10p11979, 1987.

Salby, M. L.: On the solution of the homogeneous vertical structure problem for long-period oscillations, J. Atmos. Sci., 36, 2350–2359, https://doi.org/10.1175/1520-0469(1979)036<2350:OTSOTH>2.0.CO;2, 1979.

Schindelin, J., Arganda-Carreras, I., Frise, E., Kaynig, V., Longair, M., Pietzsch, T., Preibisch, S., Rueden, C., Saalfeld, S., Schmid, B., Tinevez, J. Y., White, D. J., Hartenstein, V., Eliceiri, K., Tomancak, P., and Cardona, A.: Fiji: an open-source platform for biological-image analysis, Nat. Methods, 9, 676–682, https://doi.org/10.1038/nmeth.2019, 2012.

Sedov, L. I.: Similarity and Dimensional Methods in Mechanics, 10th edn., CRC Press, Boca Raton, FL, https://doi.org/10.1201/9780203739730, 1993.

Sepúlveda, I., Carvajal, M., and Agnew, D. C.: Global winds shape planetary-scale Lamb waves, Geophys. Res. Lett., 50, e2023GL106097, https://doi.org/10.1029/2023GL106097, 2023.

Sublette, C.: Big Ivan, The Tsar Bomba, Nuclear weapon archive, https://nuclearweaponarchive.org/Russia/TsarBomba.html (last access 4 July 2026), 2007.

Symons, G. J. (Ed.): The Eruption of Krakatoa, and Subsequent Phenomena: Report of the Krakatoa Committee of the Royal Society, Trübner & Co., London, https://archive.org/details/eruptionkrakato00whipgoog (last access: 4 July 2026), 1888.

Tahira, M., Nomura, M., Sawada, Y., and Kamo, K.: Infrasonic and acoustic-gravity waves generated by the Mount Pinatubo eruption of June 15, 1991, in: Fire and mud: Eruptions and lahars of Mount Pinatubo, Philippines, edited by: Newhall, C. G. and Punongbayan, R. S (Eds.), University of Washington Press, Seattle, London, https://pubs.usgs.gov/pinatubo/tahira/ (last access: 4 July 2026), 1996.

Taylor, G. I.: The formation of a blast wave by a very intense explosion. – II. The atomic explosion of 1945, Proc. R. Soc. Lond. A, 201, 175–186, https://doi.org/10.1098/rspa.1950.0050, 1950.

The GIMP Development Team: GIMP – GNU Image Manipulation Program, Version 3.2.4, Community Free Software (license GPLv3) [code], https://gimp.org/ (last access: 4 July 2026), 2026.

Tölle, M. H. and Krueger, S. K.: Effects of entrainment and mixing on droplet size distributions in warm cumulus clouds, J. Adv. Model. Earth Syst., 6, 281–299, https://doi.org/10.1002/2012MS000209, 2014.

Vadas, S. L., Figueiredo, C., Becker, E., Huba, J. D., Themens, D. R., Hindley, N. P., Mrak, S., Galkin, I., and Bossert, K.: Traveling ionospheric disturbances induced by the secondary gravity waves from the Tonga eruption on 15 January 2022: Modeling with MESORAC/HIAMCM/Sami3 and comparison with GPS/TEC and ionosonde data, J. Geophys. Res. Space Phys., 128, e2023JA031408, https://doi.org/10.1029/2023JA031408, 2023.

Várnai T., Marshak A., and Kostinski, A.: Statistics of glinting clouds observed by DSCOVR and geostationary satellites, Front. Remote Sens., 6, 1696519, https://doi.org/10.3389/frsen.2025.1696519, 2026.

Vergoz, J., Hupe, P., Listowski, C., Le Pichon, A., Garcés, M. A., Marchetti, E., Labazuy, P., Ceranna, L., Pilger, C., Gaebler, P., Näsholm, S. P., Brissaud, Q., Poli, P., Shapiro, N., De Negri, R., and Mialle, P.: IMS observations of infrasound and acoustic-gravity waves produced by the January 2022 volcanic eruption of Hunga, Tonga: A global analysis, Earth Planet. Sci. Lett., 591, 117639, https://doi.org/10.1016/j.epsl.2022.117639, 2022.

von Neumann, J.: The point source solution, In: Collected Works, Vol. VI.: Theory of Games, Astrophysics, Hydrodynamics and Meteorology, Pergamon Press, New York, NY, 219–237, https://z-library.sk/book/VJvekNawRE/collected-works-vol-6-theory-of-games-astrophysics (last access: 8 October 2026), 1963.

Waltz, R. E.: Wilson cloud formation by low-altitude nuclear explosions, J. Fluid Mech., 85, 787–794, https://doi.org/10.1017/S0022112078000932, 1978.

Watada, S. and Kanamori, H.: Acoustic resonant oscillations between the atmosphere and the solid earth during the 1991 Mt. Pinatubo eruption, J. Geophys. Res.-Solid Earth, 115, B12319, https://doi.org/10.1029/2010JB007747, 2010.

Watanabe, S., Hamilton, K., Sakazaki, T., and Nakano, M.: First detection of the Pekeris internal global atmospheric resonance: Evidence from the 2022 Tonga eruption and from global reanalysis data, J. Atmos. Sci., 79, 3027–3043, https://doi.org/10.1175/JAS-D-22-0078.1, 2022.

Watada, S., Imanishi, Y., and Tanaka, K.: Detection of air temperature and wind changes synchronized with the Lamb wave from the 2022 Tonga volcanic eruption, Geophys. Res. Lett., 50, e2022GL100884, https://doi.org/10.1029/2022GL100884, 2023.

Wellerstein, A.: An unearthly spectacle: The untold story of the world's biggest nuclear bomb, Bull. At. Sci., https://thebulletin.org/2021/11/the-untold-story-of-the-worlds-biggest-nuclear-bomb/ (last access: 4 July 2026), 2021.

Whitham, G. B.: The flow pattern of a supersonic projectile, Comm. Pure Appl. Math., 5, 301–348, https://doi.org/10.1002/cpa.3160050305, 1952.

Wielandt, E.: First-order asymptotic theory of the polar phase shift of Rayleigh waves, Pure Appl. Geophys., 118, 1214–1227, https://doi.org/10.1007/BF01593062, 1980.

Wright, C. J., Hindley, N. P., Alexander, M. J., Barlow, M., Hoffmann, L., Mitchell, C. N., Prata, F., Bouillon, M., Carstens, J., Clerbaux, C., Osprey, S. M., Powell, N., Randall, C. E., and Yue, J.: Surface-to-space atmospheric waves from Hunga Tonga–Hunga Ha'apai eruption, Nature, 609, 741–746, https://doi.org/10.1038/s41586-022-05012-5, 2022.

Yokoyama, I.: A geophysical interpretation of the 1883 Krakatau eruption, J. Volcanol. Geotherm. Res., 9, 359–378, https://doi.org/10.1016/0377-0273(81)90044-5, 1981.

Zéhil, G. P.: Investigating the blast shielding effect of the Beirut silos, Shock Waves, 34, 227–235, https://doi.org/10.1007/s00193-024-01189-y, 2024.